weighting scheme used in the least-squares refinements was $w = 1.17/(\sigma(F_o)^2 + 0.0020F_o^2)$. Final R and R_w were 0.056 and 0.057, respectively. The final atomic positional parameters are presented in Table VII. All the computations were performed with the SHELX-76 package on an IBM 3083 computer.

Acknowledgment. We thank Prof. S. Martinengo for his interest in this work and M. Bonfà for recording the NMR spectra.

Registry No. **1**$[PPh_4]_2$, 117469-96-2; **1**$[PPN]_2$, 117469-97-3; **1**$[NnBu_4]_2$, 117469-98-4; **2**$[NEt_4]_2$, 117470-01-6; **2**$[PPN]_2$, 117470-00-5; Na_2PtCl_6, 16923-58-3; $Ir_4(CO)_{12}$, 18827-81-1; Ir, 7439-88-5; Pt, 7440-06-4; ^{195}Pt, 14191-88-9.

Supplementary Material Available: Tables of thermal parameters for $[PPh_4]_2[PtIr_4(CO)_{14}]$ (**1**) and for $[NEt_4]_2[PtIr_4(CO)_{12}]$ (**2**), hydrogen atoms coordinates for **1** (9 pages); tables of observed and calculated structure factor amplitudes for **1** and for **2** (54 pages). Ordering information is given on any current masthead page.

Lattice-Engineered Micromodulation of Intramolecular Electron-Transfer Rates in Trinuclear Mixed-Valence Iron Acetate Complexes

Ho G. Jang,[1] Steven J. Geib,[2] Yuki Kaneko,[3] Motohiro Nakano,[3] Michio Sorai,*[,3] Arnold L. Rheingold,*[,2] Bernard Montez,[1] and David N. Hendrickson*[,1]

Contribution from the School of Chemical Sciences, University of Illinois, Urbana, Illinois 61801, Department of Chemistry, University of Delaware, Newark, Delaware 19716, and the Chemical Thermodynamics Laboratory, Faculty of Sciences, Osaka University, Toyonaka, Osaka 560, Japan. *Received June 16, 1988*

Abstract: The factors influencing the rate of intramolecular electron transfer in the solid state have been investigated for the oxo-centered, mixed-valence complexes $[Fe_3O(O_2CCH_3)_6(4\text{-Me-py})_3]S$, where S is either $CHCl_3$ (**1**), CH_3CCl_3 (**2**), CH_3CHCl_2 (**3**), or C_6H_6 (**4**), and $[Fe_3O(O_2CCH_3)_6(py)_3]S$, where S is either $CHCl_3$ (**5**) or C_5H_5N (**6**). Complex **1** crystallizes in the rhombohedral space group $R32$ with three molecules in a unit cell with dimensions a = 18.759 (6) Å, and c = 10.373 (3) Å at 298 K. The final discrepancy factors are R = 0.0323 and R_w = 0.0363 for 1166 reflections with $F_o > 5\sigma(F_o)$. The bond distances about each iron atom are Fe–O(oxide) = 1.912 (1) Å, Fe–N = 2.221 (4) Å and an average Fe–O(acetate) distance of 2.080 Å. Along the c-axis of complex **1**, Fe_3O complexes and $CHCl_3$ solvate molecules occupy alternating sites of 32 symmetry. The $CHCl_3$ solvate molecule is disordered about the three C_2 axes which are perpendicular to the C_3 axis. This disorder was modeled with the three Cl atoms in a plane, above and below which the C–H moiety was disordered with the C–H vector along the C_3 axis. Examination of the parameters (thermal and distances) resulting from this fit clearly indicates that the C–H vector of the $CHCl_3$ solvate is not just sitting on the C_3 axis but is also jumping to positions off the C_3 axis. Complex **5** also crystallizes in the $R32$ space group with Z = 3, a = 17.819 (6) Å, and c = 10.488 (3) Å at 298 K [R = 0.0327 and R_w = 0.0377 for 1373 reflections with $F_o > 5\sigma(F_o)$]. The $CHCl_3$ solvate molecules in **5** are disordered the same way as those in **1**. Substantiation for the onset of dynamic disorder of the $CHCl_3$ solvate molecules comes from heat capacity data measured for complex **5** between 14 and 300 K. A phase transition with two peaks closely centered at 207.14 and 208.19 K was found. The total transition enthalpy and entropy gain for the phase transition are ΔH = (5107 ± 44) J mol^{-1} and ΔS = (28.10 ± 0.44) JK^{-1} mol^{-1}. The entropy gain first appears at ~100 K as the temperature is increased from 14 K. The experimental ΔS can be accounted for by a combination of Fe_3O complexes converting from valence trapped in one vibronic state to dynamically converting between all four vibronic states ($\Delta S = R\ln 4$) and each of the $CHCl_3$ molecules going from static to dynamically jumping between eight positions ($\Delta S = R\ln 8$). The total $\Delta S = R\ln 32$ (= 28.82 JK^{-1} mol^{-1}) agrees with the experimental entropy gain. Variable temperature ^{57}Fe Mössbauer data are presented for all six complexes. In general, a valence-trapped spectrum with Fe^{II} and Fe^{III} doublets is seen at low temperatures. As the temperature is increased, a third doublet characteristic of an undistorted (delocalized) complex appears. Further increase in temperature changes the spectrum at a higher temperature to only a single doublet for delocalized complexes. The two temperatures for these occurrences are seen to be ~160 and ~208 K for complex **5**; the latter temperature agrees with the culmination temperature seen in the C_p data for the phase transition of complex **5**. The Mössbauer spectrum of complex **1** changes fairly abruptly with the third doublet first seen at ~81 K and the complete conversion to Mössbauer detrapped at ~90–95 K. This agrees with the DTA data for this complex which shows a peak at 95 K. It is interesting that complex **3** with its less symmetric CH_3CHCl_2 solvate molecule becomes valence detrapped on the Mössbauer time scale at 45° higher temperature than for the CH_3CCl_3 solvate **2**. A magnetically oriented sample of 20 small crystals of $CDCl_3$ solvate **5** in a wax block was employed with solid-state ^2H NMR spectroscopy to probe the dynamics of the chloroform solvate molecule. With the magnetic field directed down the c-axis the quadrupole splitting of the single ^2H NMR doublet remained relatively constant (196–204 kHz) in the range 295–208 K and then decreased below the phase transition temperature at 208 K to become eventually 144 kHz at 110 K. Above 208 K the $CDCl_3$ solvate molecule is jumping between eight positions, four with the C–D vector pointed up and four down, where for the four up positions one C–D vector position is along the c-axis and the other three are at an angle of 24.7° relative to the c-axis. At 110 K the C–D vector is static and takes only one position at an angle of 31.5° from the c-axis. The nature of the phase transitions seen for each of the **1**–**6** complexes is discussed. Intermolecular pyridine–pyridine ligand overlaps appear to be important in determining where the phase transition from a valence-trapped to a valence-detrapped state occurs. The solvate molecules, one above and one below each Fe_3O complex, also likely affect the rate of intramolecular electron transfer in each Fe_3O complex as the solvate molecules go from static to dynamic. The experimental results in this paper are compared to the predictions of a theoretical model based on a molecular field calculation.

Variations in environmental conditions can dramatically affect electron-transfer processes in chemical and biological systems.[4] It is not known, for example, what influence the dynamics of water and/or amino acid groups which comprise an electron-transfer

0002-7863/89/1511-0173$01.50/0

pathway between redox sites in two contiguous electron-transport proteins have on the rate of electron transfer. It is not easy to characterize environmental effects in complicated chemical or biological systems. However, the study of intramolecular electron-transfer events in binuclear or trinuclear mixed-valence metal complexes in the condensed phase may directly give fundamental information about environmental effects. With detailed structural, spectroscopic, and thermodynamic data on mixed-valence complexes it is possible to characterize the effects on the rate of intramolecular electron transfer of environmental factors such as the symmetry of the environment and the onset of dynamics associated with ligands, solvate molecules, and counterions. Recent studies of mixed-valence trinuclear iron acetate complexes[5] and binuclear biferrocenium complexes[6] clearly indicate that the detailed nature of the solid-state environment about a mixed-valence complex is probably the most important factor determining the rate of intramolecular electron transfer. Intramolecular electronic and vibronic interactions are important, but it is the environment which can turn on or off electron transfer in a mixed-valence complex.

Triangular mixed-valence complexes of the composition $[Fe_3O(O_2CCH_3)_6(L)_3]S$, where L is a ligand such as H_2O or (substituted) pyridine and S is a solvate molecule, are of use in understanding how a nearby solvate molecule can influence rates of electron transfer. At the outset it should be noted that IR studies[7] have shown that these Fe_3O complexes are trapped on the vibrational time scale and therefore have potential energy barriers for electron transfer. Early studies[5a,b] of these complexes showed that simply changing the solvate molecule changed the rate of intramolecular electron transfer. As determined by ^{57}Fe Mössbauer spectroscopy, the nonsolvated pyridine (py) complex $[Fe_3O(O_2CCH_3)_6(py)_3]$ does not valence detrap up to temperatures of 315 K, whereas the solvated complex $[Fe_3O(O_2CCH_3)_6(py)_3](py)$ is valence-detrapped on the Mössbauer time scale when the temperature is increased above 190 K. For several of these mixed-valence Fe_3O complexes it has been found that the valence detrapping occurs in a phase transition which also involves the cooperative onset of ligand and/or solvate molecule dynamics. Heat capacity data,[5c,d,j] multiple temperature X-ray structural analyses,[5b,h] and ^{57}Fe Mössbauer[5a-c,e,g,h] and solid-state ^2H NMR[5c,e,g,h] data have been used to probe these phase transitions, the nature of which has also been addressed in two theoretical papers.[5f,8]

The solvate molecule in these mixed-valence Fe_3O complexes can affect the rate of intramolecular electron transfer in basically two different ways. First, the size and shape of the solvate molecule affects the magnitude of intermolecular interactions between Fe_3O complexes. For example, in the series $[Fe_3O(O_2CCH_3)_6(py)_3]S$ (S = C_6H_6, C_5H_5N, etc.) the triangular Fe_3O complexes are arranged in stacks with the solvate molecule S sandwiched between Fe_3O complexes. Appreciable intermolecular interactions exist between a Fe_3O complex in one stack and Fe_3O complexes in the three nearest stacks. Overlapping of pyridine ligands between neighboring Fe_3O complexes lead to these intermolecular interactions. Obviously the size and shape of the solvate molecule can affect this py···py contact. This dramatically influences the rate of intramolecular electron transfer in each Fe_3O complex because the presence of intermolecular interactions lead to zero-point energy differences between the vibronic states of a Fe_3O complex. When the environment (i.e., intermolecular interactions) about a Fe_3O complex makes the zero-point energy differences between the $Fe_a^{II}Fe_b^{III}Fe_c^{III}$, $Fe_a^{III}Fe_b^{II}Fe_c^{III}$, and $Fe_a^{III}Fe_b^{III}Fe_c^{II}$ vibronic states appreciable, then the rate of tunneling between the vibronic states will be decreased.[5i]

The second and more interesting manner in which the solvate molecule S in a mixed-valence Fe_3O complex can influence the rate of electron transfer is more subtle than the first. In the stacks of complexes in $[Fe_3O(O_2CCH_3)_6(py)_3]S$ each Fe_3O complex is surrounded by two solvate molecules—a small part of a solvation sphere of a solution species. If the solvate molecule–Fe_3O van der Waals interactions lead to an environment about the Fe_3O complex which is of lower symmetry than C_3, then these van der Waals interactions will also introduce nonzero zero-point energy differences between the vibronic states of the Fe_3O complex. Again this will influence the rate of tunneling (electron transfer) of the Fe_3O complex.

In this paper results are presented for the isostructural complexes $[Fe_3O(O_2CCH_3)_6(4\text{-Me-py})_3]S$ (S = C_6H_6, $CHCl_3$, CH_3CCl_3, or CH_3CHCl_2) and $[Fe_3O(O_2CCH_3)_6(py)_3]S$ (S = C_5H_5N or $CHCl_3$). It was of interest to see whether the symmetry of the solvate molecule S, and therefore its instantaneous van der Waals interactions with neighboring Fe_3O complexes, affects the rate of electron transfer in the Fe_3O complex. Also, there is interest in whether the onset of dynamics associated with the solvate molecule S which may occur in a phase transition affect the Fe_3O electron-transfer rate. A phase transition serves to magnify the thermodynamic and spectroscopic consequences of an intramolecular electron transfer event.

Experimental Section

^{57}Fe Mössbauer Spectroscopy. Variable-temperature spectra were obtained in vertical transmission geometry by using a constant acceleration spectrometer which has been described before.[9] The sample temperature was controlled by a Lake Shore Cryotronics Model DRC80C temperature controller in conjunction with a silicon diode mounted on the copper sample cell holder and is estimated to have an absolute accuracy of ±3 K. Computer fittings of the Mössbauer data to Lorentzian line shapes were carried out with a modified version of a previously reported computer program.[10] The isomer shift values are reported relative to iron foil at 298 K but are not corrected for the temperature-dependent second-order Doppler shift.

Differential Thermal Analysis (DTA). Preliminary observation of the thermal properties were made with a home-built DTA apparatus which operates between 60 and 530 K. The mass of a compound used for a probe was about 300 mg.

(1) University of Illinois.
(2) University of Delaware.
(3) Osaka University.
(4) For recent reviews, see: (a) DeVault, D. *Quantum-Mechanical Tunneling in Biological Systems*, 2nd ed.; Cambridge University Press: Cambridge, 1984. (b) Cannon, R. D. *Electron Transfer Reactions*; Butterworths: Boston, 1980. (c) Marcus, R. A.; Sutin, N. *Biochim. Biophys. Acta* **1985**, *811*, 265. (d) Mikkelsen, K. V.; Ratner, M. A. *Chem. Rev.* **1987**, *87*, 113.
(5) (a) Oh, S. M.; Hendrickson, D. N.; Hassett, K. L.; Davis, R. E. *J. Am. Chem. Soc.* **1984**, *106*, 7984. (b) Oh, S. M.; Hendrickson, D. N.; Hassett, K. L.; Davis, R. E. *J. Am. Chem. Soc.* **1984**, *107*, 8009. (c) Oh, S. M.; Kambara, T.; Hendrickson, D. N.; Sorai, M.; Kaji, K.; Woehler, S. E.; Wittebort, R. J. *J. Am. Chem. Soc.* **1985**, *107*, 5540. (d) Sorai, M.; Kaji, K.; Hendrickson, D. N.; Oh, S. M. *J. Am. Chem. Soc.* **1986**, *108*, 702. (e) Woehler, S. E.; Wittebort, R. J.; Oh, S. M.; Hendrickson, D. N.; Inniss, D.; Strouse, C. E. *J. Am. Chem. Soc.* **1986**, *108*, 2938. (f) Kambara, T.; Hendrickson, D. N.; Sorai, M.; Oh, S. M. *J. Chem. Phys.* **1986**, *85*, 2895. (g) Woehler, S. E.; Wittebort, R. J.; Oh, S. M.; Kambara, T.; Hendrickson, D. N.; Inniss, D.; Strouse, C. E. *J. Am. Chem. Soc.* **1987**, *109*, 1063. (h) Oh, S. M.; Wilson, S. R.; Hendrickson, D. N.; Woehler, S. E.; Wittebort, R. J.; Inniss, D.; Strouse, C. E. *J. Am. Chem. Soc.* **1987**, *109*, 1073. (i) Hendrickson, D. N.; Oh, S. M.; Dong, T.-Y.; Kambara, T.; Cohn, M. J.; Moore, M. F. *Comments Inorg. Chem.* **1985**, *4*, 329. (j) Sorai, M.; Shiomi, Y.; Hendrickson, D. N.; Oh, S. M.; Kambara, T. *Inorg. Chem.* **1987**, *26*, 223.
(6) (a) Dong, T.-Y.; Cohn, M. J.; Hendrickson, D. N.; Pierpont, C. G. *J. Am. Chem. Soc.* **1985**, *107*, 4777. (b) Cohn, M. J.; Dong, T.-Y.; Hendrickson, D. N.; Geib, S. J.; Rheingold, A. L. *J. Chem. Soc., Chem. Commun.* **1985**, 1095. (c) Dong, T.-Y.; Hendrickson, D. N.; Iwai, K.; Cohn, M. J.; Rheingold, A. L.; Sano, H.; Motoyama, I.; Nakashima, S. *J. Am. Chem. Soc.* **1985**, *107*, 7996. (d) Dong, T.-Y.; Hendrickson, D. N.; Pierpont, C. G.; Moore, M. F. *J. Am. Chem. Soc.* **1986**, *108*, 963. (e) Moore, M. F.; Wilson, S. R.; Cohn, M. J.; Dong, T.-Y.; Mueller-Westerhoff, U. T.; Hendrickson, D. N. *Inorg. Chem.* **1985**, *24*, 4559. (f) Dong, T.-Y.; Kambara, T.; Hendrickson, D. N. *J. Am. Chem. Soc.* **1986**, *108*, 4423. (g) Dong, T.-Y.; Kambara, T.; Hendrickson, D. N. *J. Am. Chem. Soc.* **1986**, *108*, 5857. (h) Sorai, M.; Nishimori, A.; Hendrickson, D. N.; Dong, T.-Y.; Cohn, M. J. *J. Am. Chem. Soc.* **1987**, *109*, 4266. (i) Kambara, T.; Hendrickson, D. N.; Dong, T.-Y.; Cohn, M. J. *J. Chem. Phys.* **1987**, *86*, 2362.
(7) (a) Cannon, R. D.; Montri, L.; Brown, D. B.; Marshall, K. M.; Elliott, C. M. *J. Am. Chem. Soc.* **1984**, *106*, 2591. (b) Meesuk, L.; Jayasooriya, U. A.; Cannon, R. D. *Spectrochim. Acta* **1987**, 43A. (c) Meesuk, L.; Jayasooriya, U. A.; Cannon, R. D. *J. Am. Chem. Soc.* **1987**, *109*, 2009.
(8) Stratt, R. M.; Adachi, S. H. *J. Chem. Phys.* **1987**, *86*, 7156.
(9) Cohn, M. J.; Timken, M. D.; Hendrickson, D. N. *J. Am. Chem. Soc.* **1984**, *106*, 6683.
(10) Chrisman, B. L.; Tumolillo, T. A. *Comput. Phys. Commun.* **1971**, *2*, 322.

Table I. Crystallographic Data for $[Fe_3O(O_2CCH_3)_6(4\text{-Me-py})_3](CHCl_3)$ (**1**) and $[Fe_3O(O_2CCH_3)_6(py)_3](CHCl_3)$ (**5**)

compound	complex **1**	complex **5**
cryst system	rhombohedral	rhombohedral
space group	$R32$	$R32$
a, Å	18.759 (6)	17.819 (6)
c, Å	10.373 (3)	10.488 (3)
V, Å^3	3161 (2)	2884.2 (9)
Z	3	3
D (calcd), g cm^{-3}	1.49	1.54
temp, °C	25	25
cryst dimensions, mm	0.25 × 0.35 × 0.40	0.40 × 0.40 × 0.40
radiation, Å	Mo Kα, 0.71073	Mo Kα, 0.71073
scan speed, deg/min	variable, 6–20	variable, 6–20
scan mode	ω	ω
scan limit, deg	$4 \le 2\theta \le 50$	$4 \le 2\theta \le 50$
R (int), %	1.97	2.01
unique data	1696	1641
unique data, $F_o \ge 5\sigma(F_o)$	1166	1373
R_F, %	3.23	3.27
R_{wF}, %	3.63	3.77
goodness of fit	1.262	1.072
$\Delta(\rho)$e Å^{-3}	0.37	0.69
N_o/N_v	13.3	14.9

Heat Capacity Measurements. Heat capacities were measured with an adiabatic calorimeter cell[11] made of gold-plated copper which was loaded with 15.6245 g (0.01746750 mol) of polycrystalline $[Fe_3O(O_2CCH_3)_6(py)_3](CHCl_3)$ with buoyancy correction assuming a density of 1.34 g cm^{-3}. A small amount of helium gas was sealed in the cell to aid in heat transfer. Considerable additional details of the data collection and analysis are available in a full report[12] on the heat capacity of $[Fe_3O(O_2CCH_3)_6(py)_3](CHCl_3)$.

Solid-State ^{2}H NMR Spectroscopy. ^{2}H NMR spectra were obtained on a "home-built" spectrometer operating at 55.3 MHz with an 8.45 T, 3.0 in bore Oxford Instruments superconducting solenoid, a Nicolet Model 1280 computer, and a 2090 transient recorder. We also used a home-built solenoidal radio frequency coil probe (sample volume ~0.8 cm^3). The pulse sequence was a standard quadrupole echc sequence $[(90)_x\text{–}t\text{–}(90)_y\text{–}t\text{–}\text{observe}]$ for data acquisition. The value of t = 50 μs and a 90° pulse width of 3.3 μs were used. In the case of a magnetically oriented sample, several crystals were suspended in fluid eicosane (mp = 38 °C) at 50 °C while the crystals were oriented by the 8.45 T magnetic field such that the principal axis of the magnetic susceptibility tensor of each crystal was aligned with the magnetic field. The hydrocarbon matrix was then slowly cooled to room temperature to form a solid block with the crystals embedded in it. The random power sample was prepared by mixing the powder sample in the melted hydrocarbon matrix(eicosane) outside the magnetic field and then cooling it to room temperature.

Crystal Measurements, Data Collection, and X-ray Structure Refinement for $[Fe_3O(O_2CCH_3)_6(4\text{-Me-py})_3](CHCl_3)$ (1). A black crystal (0.25 × 0.35 × 0.40 mm) was grown by slow evaporation under Ar of a $CHCl_3$ solution of **1**. Systematic absences in the intensity data and diffraction symmetry determined for **1** the rhombohedral space groups $R32$, $R\bar{3}m$, or $R3m$. Both statistics based upon E values and knowledge of the molecular symmetry of **1** initially suggested that $R32$ was the correct space group; the chemically reasonable and well-behaved solution and refinement of the structure proved this choice correct. Data were collected at 298 K on a Nicolet R3 automated diffractometer. Details of data collection may be found in Table I. No evidence of crystal decomposition was noted (decay ≤ 0.5%). The unit cell parameters, listed in Table I, were obtained by a least-squares fit to the automatically centered settings of 25 reflections, $22° \le 2\theta \le 26°$. The data were corrected for Lorentz, polarization, and anomalous dispersion effects. The data were also corrected empirically for absorption (max/min transm = 0.58/0.46).

The structure of **1** was solved by an interpreted Patterson procedure which located the Fe atom; the remaining non-hydrogen atoms were obtained from subsequent difference Fourier syntheses. The asymmetric unit consists of 1/6 of the Fe_3 complex and 1/3 of a $CHCl_3$ solvate molecule, each situated on a crystallographic 32 site. The disordered $CHCl_3$ molecule was modeled by placing three 1/3 Cl atoms in a plane, above and below which were located two 1/6 occupancy C atoms to form a trigonal bipyramidal configuration. The nature of the disorder in this $CHCl_3$ molecule is commented on more fully in the Results and Discussion section. A multiplicative factor for Δf[11] was refined to 1.06 (6) indicating that the enantiomorph reported is correct.

Refinement of the structure of **1** by blocked cascade procedures included anisotropic temperature factors for non-hydrogen atoms and hydrogen atoms that were incorporated as fixed idealized isotropic contributions [d(C–H) = 0.96 Å]. Atomic coordinates are given in Table II.

All computer programs used are contained in the diffractometer (P3) and SHELXTL (version 5.1) program libraries distributed by the Nicolet Corp.

Crystal Measurements, Data Collection, and X-ray Structure Refinement for $[Fe_3O(O_2CCH_3)_6(py)_3](CHCl_3)$, 5. A black crystal (0.40 × 0.40 × 0.40 mm) was grown by slow evaporation under Ar of a $CHCl_3$ solution of **5**. Complex **5** was found to be isostructural to complex **1** and, thus, data collection (see Table I) and structure refinement were carried out in the same manner as described for complex **1**. Atomic coordinates are given in Table III.

Compound Preparations. 4-Methylpyridine was dried by refluxing over BaO and fractionally distilled under an argon atmosphere. Benezene was dried with Na/benzophenone and distilled. Chloroform (99+%), deuteriated chloroform 99.8 atm %D), and trichloroethane (99+%) were used without further purification. All elemental analyses were performed in the Microanalytical Laboratory of the School of Chemical Sciences, University of Illinois. Purified solvents and dried compounds were always stored and manipulated under an argon atmosphere.

$[Fe_3O(O_2CCH_3)_6(H_2O)_3]$. This mixed-valence compound was prepared according to a modification of a previously reported method.[13] A solution of 30 g (0.15 mol) of $FeCl_2 \cdot 4H_2O$ in 150 mL of water was placed in a 500 mL, three-necked flask. A suspension of 30 g (0.366 mol) of CH_3COONa and 90 mL (1.57 mol) of glacial acetic acid was added.

Table II. Positional Parameters for $[Fe_3O(O_2CCH_3)_6(4\text{-Mepy})_3](CHCl_3)$ (**1**)

atom	x/a	y/b	z/c
Fe	0.8981 (1)	0.8981 (1)	0.5000
O(1)	0.8375 (2)	0.9369 (2)	0.6284 (3)
O(2)	0.9188 (2)	1.0727 (2)	0.6503 (3)
O(3)	1.0000	1.0000	0.5000
N	0.7797 (2)	0.7797 (2)	0.5000
C(1)	0.8553 (2)	1.0050 (2)	0.6756 (4)
C(2)	0.7880 (3)	0.9921 (3)	0.2293 (4)
C(3)	0.7074 (2)	0.7774 (3)	0.4918 (4)
C(4)	0.6317 (3)	0.7054 (3)	0.4938 (4)
C(5)	0.6299 (3)	0.6299 (3)	0.5000
C(6)	0.5507 (3)	0.5507 (3)	0.5000
C(7)	0.0000	0.0000	0.6090 (18)
Cl	0.0000	0.0893	0.0000
H(2a)	0.7499	0.9534	0.7825
H(2b)	0.7767	1.0432	0.7825
H(2c)	0.8229	1.0289	0.7378
H(3)	0.7080	0.8286	0.4836
H(4)	0.5815	0.7073	0.4914
H(6a)	0.5615	0.5058	0.5048
H(6b)	0.5211	0.5462	0.4221
H(6c)	0.5184	0.5489	0.5731

Table III. Positional Parameters for $[Fe_3O(O_2CCH_3)_6(py)_3](CHCl_3)$ (**5**)

atom	x/a	y/b	z/c
Fe	0.1068 (1)	0.1068 (1)	−0.5000
O(3)	0.0000	0.0000	−0.5000
O(1)	0.0695 (2)	0.1661 (2)	−0.6354 (3)
O(2)	−0.0740 (2)	0.0905 (2)	−0.6425 (3)
N	0.2315 (2)	0.2315 (2)	−0.5000
C(1)	−0.0019 (2)	0.1509 (2)	−0.6769 (4)
C(2)	−0.0030 (3)	0.2101 (3)	−0.7775 (4)
C(3)	0.2339 (2)	0.3068 (3)	−0.5110 (4)
C(4)	0.3095 (3)	0.3852 (3)	−0.5147 (4)
C(5)	0.3862 (3)	0.3862 (3)	−0.5000
C(6)	0.0000	0.0000	−0.063 (2)
Cl	−0.0926 (2)	0.0000	0.0000

(11) Sorai, M.; Kaji, K., construction of an adiabatic calorimeter capable of measuring heat capacities between 12 and 530 K, unpublished results.

(12) Kaneko, Y.; Nakano, M.; Sorai, M.; Hendrickson, D. N.; Jang, H. G. Submitted for publication.

(13) Johnson, M. K.; Cannon, R. D.; Powell, D. B. *Spectrochim. Acta* **1982**, *38A*, 307.

The reaction mixture was heated at 70–75 °C under reflux for 2 h with bubbling of a constant stream of air. The mixture was cooled to room temperature, and the dark-brown precipitate was filtered, washed with ethanol and ethyl ether, and dried under vacuum for 3 days. The yield was 15.6 g (52.7%).

$[Fe_3O(O_2CCH_3)_6(4\text{-Me-py})_3](4\text{-Me-py})$. The sample of this compound was prepared by the method Ripan and Lupu[14] used for the preparation of $\{Fe_3O(O_2CCH_3)_6(py)_3\}py$. $[Fe_3O(O_2CCH_3)_6(H_2O)_3]$ (5.0 g, 8.5 mmol) was dissolved in 30 mL of 4-methylpyridine and stirred for 1 h at 60–65 °C under an argon atmosphere. A small amount of insoluble solid was filtered off. The solution was then cooled to room temperature and slowly evaporated for 3 days. The black crystalline product was filtered off and dried under vacuum [yield was 5.49 g (71.0%)]. Anal. Calcd for $C_{36}H_{46}N_4Fe_3O_{13}$: C, 47.50; H, 5.06; N, 6.16; Fe, 18.41. Found: C, 47.66; H, 5.16; N, 6.41; Fe, 17.76.

$[Fe_3O(O_2CCH_3)_6(4\text{-Me-py})_3](C_6H_6)$. This compound was also prepared by recrystallizing 5.0 g (5.5 mmol) of $[Fe_3O(O_2CCH_3)_6(4\text{-Me-py})_3](4\text{-Me-py})$ in 30 mL of benzene and then slowly evaporating for 2 days under an argon atmosphere. The black crystalline product was filtered off and dried briefly under vacuum [yield was 3.4 g (69%)]. Anal. Calcd for $C_{36}H_{45}N_3Fe_3O_{13}$: C, 48.30; H, 5.07; N, 4.69; Fe, 18.71. Found: C, 47.87; H, 5.03; N, 4.65; Fe, 18.55.

$[Fe_3O(O_2CCH_3)_6(4\text{-Me-py})_3](CHCl_3)$, $[Fe_3O(O_2CCH_3)_6(4\text{-Me-py})_3](CH_3CCl_3)$, and $[Fe_3O(O_2CCH_3)_6(4\text{-Me-py})_3](CH_3CHCl_2)$ were prepared by recrystallizing 2.0 g (2.2 mmol) of $[Fe_3O(O_2CCH_3)_6(4\text{-Me-py})_3](4\text{-Me-py})$ in 50 mL of $CHCl_3$, CH_3CCl_3, or CH_3CHCl_2, respectively. Each reaction mixture was heated at 50 °C for 1 h, and the insoluble solid was filtered off with Schlenk tubes. The filtrate was slowly evaporated for 2–3 days under an argon atmosphere. Anal. Calcd for $[Fe_3O(O_2CCH_3)_6(4\text{-Me-py})_3](CHCl_3)$: C, 39.76; H, 4.31; N, 4.49; Fe, 17.89; Cl, 11.36. Found: C, 39.57; H, 4.44; N, 4.28; Fe, 17.66; Cl, 11.35. Anal. Calcd for $[Fe_3O(O_2CCH_3)_6(4\text{-Me-py})_3](CH_3CCl_3)$: C, 40.43; H, 4.42; N, 4.42; Fe, 17.62; Cl, 11.21. Found: C, 40.39; H, 4.52; N, 4.37; Fe, 17.54; Cl, 11.13. Anal. Calcd for $[Fe_3O(O_2CCH_3)_6(4\text{-Me-py})_3](CH_3CHCl_2)$: C, 41.95; H, 4.70; N, 4.59; Fe, 18.29; Cl, 7.76. Found: C, 41.90; H, 4.77; N, 4.57; Fe, 18.49; Cl, 7.96.

$[Fe_3O(O_2CCH_3)_6(py)_3](CHCl_3)$. This mixed-valence compound was prepared by the same procedure as above except in the recrystallization 2.0 g of $[Fe_3O(O_2CCH_3)_6(py)_3](py)$ were dissolved in 40 mL of $CHCl_3$. Anal. Calcd for $C_{28}H_{34}N_3Fe_3O_{13}Cl_3$: C, 37.60; H, 3.83; N, 4.71; Fe, 18.73; Cl, 11.89. Found: C, 37.67; H, 3.85; N, 4.98; Fe, 18.58; Cl, 12.00.

Results and Discussion

Compound Preparation and Strategy. The goal of this study was to prepare several mixed-valence $[Fe_3O(O_2CCH_3)_6(L)_3]S$ complexes which are isostructural and where only the solvate molecule S is changed from one member to another in a given series. With such series of complexes we can potentially discover what influence the solvate molecule S has on the rate of intramolecular electron transfer. All of the compounds in the following two series crystallize in the $R32$ space group:

$$[Fe_3O(O_2CCH_3)_6(4\text{-Me-py})_3]S$$
$$S = CHCl_3\ (\mathbf{1})$$
$$S = CH_3CCl_3\ (\mathbf{2})$$
$$S = CH_3CHCl_2\ (\mathbf{3})$$
$$S = C_6H_6\ (\mathbf{4})$$

$$[Fe_3O(O_2CCH_3)_6(py)_3]S$$
$$S = CHCl_3\ (\mathbf{5})$$
$$S = C_5H_5N\ (\mathbf{6})$$

The single-crystal X-ray structures of complexes **4** and **6** have already been reported[5e,g] to have the $R32$ space group symmetry. The results of the single-crystal X-ray structures of complexes **1** and **5** reported in this paper also confirm that these two complexes have $R32$ symmetry. It is important to have the $R32$ symmetry because it is this packing arrangement which is treated in the theoretical modeling[5f,8] of phase transitions in these Fe_3O complexes. Room temperature powder X-ray diffraction patterns for complexes **1–4** are shown in Figure 1. From these patterns it is reasonable to conclude that the CH_3CCl_3 and CH_3CHCl_2 solvates are isostructural to the $CHCl_3$ solvate.

In the 4-Me-py series the influence of lowering the symmetry of the solvate molecule can be examined. If the C–H vector of a $CHCl_3$ solvate molecule is collinear with the C_3 symmetry axis of nearby Fe_3O complexes, then the environment about the Fe_3O complex will have C_3 symmetry. A C_3 symmetry environment also results if the C–C vector in the CH_3CCl_3 solvate is collinear with the C_3 axis of nearby Fe_3O complexes. In the CH_3CHCl_2 solvate **3** it is necessary that there be rotation about the C–C bond in order for the environment of the Fe_3O complex to have an effective C_3 symmetry. The plane of the C_6H_6 solvate molecule is perpendicular to the Fe_3O plane in complex **4**. It is known from the X-ray structure[5e] of **4** that each C_6H_6 solvate is 3-fold disordered about the C_3 axis which runs through neighboring Fe_3O complexes. It is plausible that the onset of a dynamical disorder of the C_6H_6 solvate molecules, where each C_6H_6 molecule jumps between three positions, leads to a C_3 symmetry environment and a valence detrapping of the Fe_3O complexes.

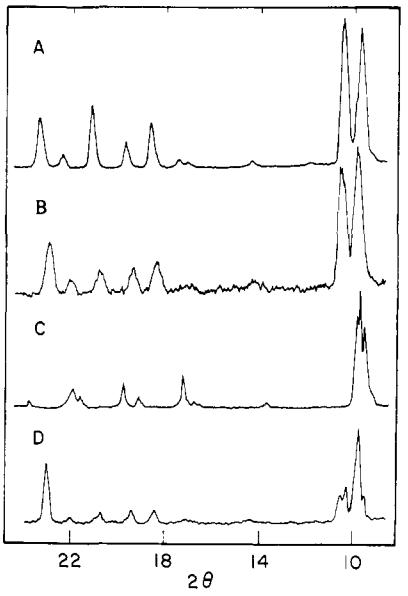

Figure 1. Room temperature powder X-ray diffraction patterns for the following: A, $[Fe_3O(O_2CCH_3)_6(4\text{-Me-py})_3](CHCl_3)$; B, $[Fe_3O(O_2CCH_3)_6(4\text{-Me-py})_3](CH_3CHCl_2)$; C, $[Fe_3O(O_2CCH_3)_6(4\text{-Me-py})_3](C_6H_6)$; D, $[Fe_3O(O_2CCH_3)_6(4\text{-Me-py})_3](CH_3CCl_3)$.

Table IV. Selected Bond Distances (Å) and Angles (deg) of the Central Atoms for $[Fe_3O(O_2CCH_3)_6(4\text{-Me-py})_3](CHCl_3)$ (**1**) at 297 K

atoms	distances (Å)	atoms	distances (Å)
Fe–O(3)	1.912 (1)	C(1)–C(2)	1.510 (8)
Fe–O(1)	2.105 (3)	C(3)–N	1.337 (5)
Fe–O(2a)	2.054 (3)	C(3)–C(4)	1.386 (5)
Fe–O(2c)	2.054 (3)	C(4)–C(5)	1.403 (6)
Fe–N	2.221 (4)	C(5)–C(6)	1.485 (8)
C(1)–O(1)	1.247 (5)	C(7)–Cl	1.791 (7)
C(1)–O(2)	1.260 (4)	C(7)–C(7a)	1.264 (37)
atoms	**angles (deg)**	**atoms**	**angles (deg)**
Fe–O(3)–Fe	120	O(2a)–Fe–O(2c)	168.0 (1)
O(3)–Fe–N	180	O(1)–Fe–O(2c)	90.2 (1)
O(3)–Fe–O(1)	95.6 (1)	O(1e)–Fe–O(2a)	88.7 (1)
O(3)–Fe–O(2a)	96.0 (1)	O(1)–Fe–N	84.4 (1)
O(1)–Fe–O(1e)	168.9 (1)	O(2a)–Fe–N	84.0 (1)

X-ray Structures of $[Fe_3O(O_2CCH_3)_6(4\text{-Me-py})_3](CHCl)_3$ and $[Fe_3O(O_2CCH_3)_6(py)_3](CHCl_3)$. The molecular and solid-state structures of complexes **1** and **5** were determined at 298 K by single-crystal X-ray diffraction techniques. These two complexes crystallize in the space group $R32$ with $Z = 3$. Drawings of the molecular structures of complexes **1** and **5** are shown in Figure 2. In both cases the triply bridging oxygen atom resides at a site of 32 symmetry. The central O^{2-} ion, the three iron atoms, and the three pyridine N atoms lie exactly in a plane. As found for complex **5**, the Fe–O(oxide) distance [1.912 (1) Å] in complex **1** is intermediate between the average Fe^{III}–O [1.862 (4) Å] and the Fe^{II}–O [2.006 (4) Å] distances found[15] at 298 K for the toluene

(14) Lupu, D.; Ripan, R. *Rev. Roum. Chim.* **1971**, *16*, 43.

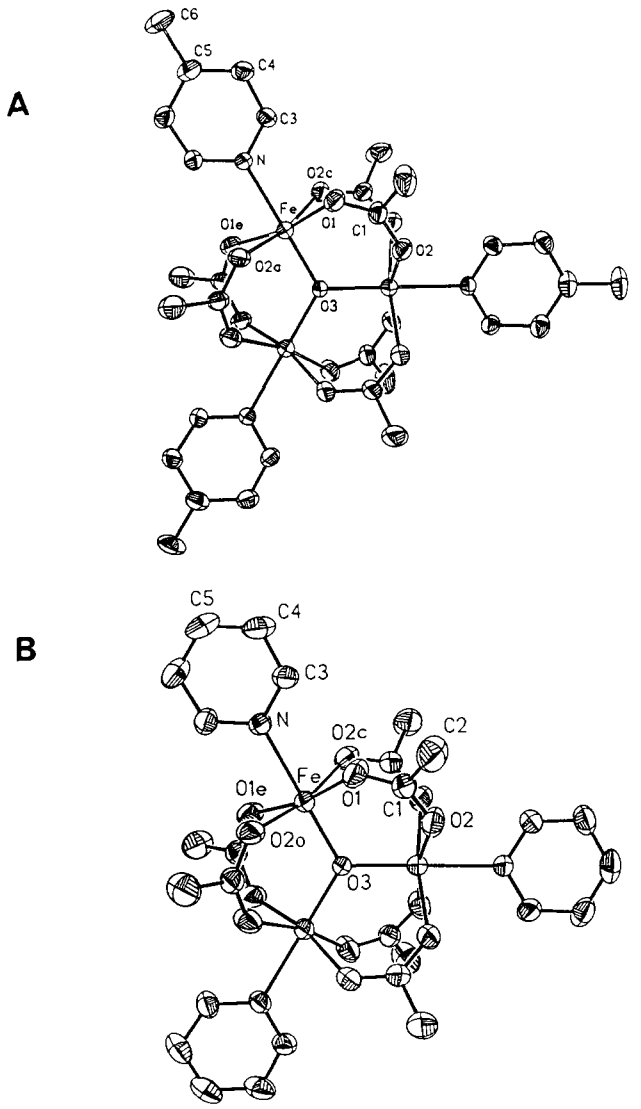

Figure 2. ORTEP plots of the molecular structures of the Fe_3O complexes in (A) $[Fe_3O(O_2CCH_3)_6(4\text{-Me-py})_3](CHCl_3)$ (**1**) and (B) $[Fe_3O(O_2CCH_3)_6(py)_3](CHCl_3)$ (**5**). Atoms are shown as 50% equiprobability ellipsoids.

Table V. Selected Bond Distances (Å) and Angles (deg) of the Central Atoms for $[Fe_3O(O_2CCH_3)_6(py)_3](CHCl_3)$ (**5**) at 297 K

atoms	distances (Å)	atoms	distances (Å)
Fe–O(3)	1.903 (1)	C(1)–C(2)	1.499 (8)
Fe–O(1)	2.069 (3)	C(3)–N	1.326 (5)
Fe–O(2a)	2.058 (3)	C(3)–C(4)	1.373 (7)
Fe–O(2c)	2.058 (4)	C(4)–C(5)	1.367 (7)
Fe–N	2.222 (4)	C(6)–O(1)	4.075 (5)
C(1)–O(1)	1.239 (6)	C(6)–O(2)	3.996 (5)
C(1)–O(2)	1.246 (6)	C(6)–O(3)	4.578 (5)
atoms	**angles (deg)**	**atoms**	**angles (deg)**
Fe–O(3)–Fe	120	O(1)–Fe–O(2c)	88.9 (1)
O(3)–Fe–N	179.9	O(1e)–Fe–O(2a)	89.9 (1)
O(3)–Fe–O(1)	95.4 (1)	O(1)–Fe–N	84.6 (1)
O(3)–Fe–O(2a)	96.2 (1)	O(2a)–Fe–N	83.8 (1)
O(1)–Fe–O(1e)	169.1 (1)	O(1)–C(6)–O(3)	39.2 (1)
O(2a)–Fe–O(2c)	167.6 (1)	O(2)–C(6)–O(3)	39.5 (1)

solvate $[Fe_3O(O_2CCH_3)_6(3\text{-Et-py})_3]\cdot{}^1/_2(C_6H_5CH_3)$, a complex which is known[15] to be valence trapped not only at low temperatures but also at 350 K. In Tables IV and V are given bond distances and angles of the central atoms for the complexes **1** and **5**. These dimensions are essentially the same as those reported for complexes **4** and **6** and it can be concluded that the central Fe_3O cores of the valence-detrapped forms of complexes **1**–**6** likely all are essentially identical. As a result of internal twinning (presumably due to domain structure), it has not proved possible to determine the structure of **1**, **4**, **5**, **6**, or isostructural $[Mn_3O(O_2CCH_3)_6(py)_3](py)$[16] at temperatures below the phase transitions seen for these complexes.

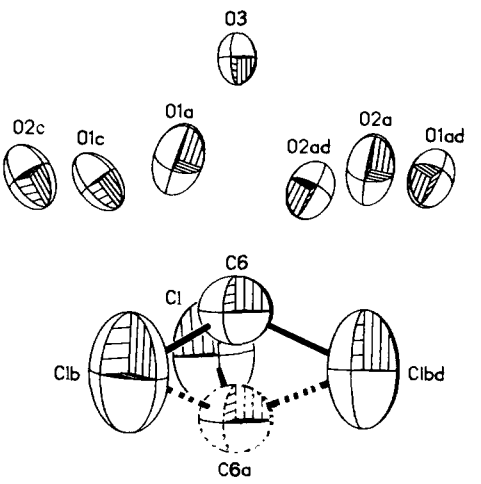

Figure 3. ORTEP view of the $CHCl_3$ solvate molecule environment in $[Fe_3O(O_2CCH_3)_6(py)_3](CHCl_3)$ (**5**). The disorder in the $CHCl_3$ solvate was modeled by having the C(6)–H moiety (H atom is not shown) disordered above and below a triangle of Cl atoms. The C(6)–H vector in the model was assumed to be along the C_3 axis (*c*-axis). Six acetate O atoms and the oxide ion, O(3) that are facing toward the $CHCl_3$ solvate molecule are shown.

The packing arrangements for complexes **1** and **5** are the same as found for **4** and **6**. Along the *c*-axis of **1** and **5**, Fe_3O complexes and $CHCl_3$ solvate molecules occupy alternating sites of 32 symmetry.

The disposition of the $CHCl_3$ solvate molecules in complexes **1** and **5** is important to the present study. Since the solvate molecule situations in these two complexes are similar, only the results of modeling the disordered $CHCl_3$ in **5** will be described. In a difference Fourier map it was found that the three Cl atoms of **1** form a plane. The –CH moiety appeared to be disordered on the C_3 axis above and below the triangle of Cl atoms. Refinement of this model converged to the $CHCl_3$ atom positions given in Table III. A view of the disordered $CHCl_3$ solvate molecule minus the H atom is given in Figure 3. In this figure are also shown the central O^{2-} ion and the six downward-facing acetate O atoms from one neighboring Fe_3O complex. These atoms line the cavity into which the chloroform C–H vector points. The contact distances are C(6)–O(1) = 4.075, C(6)–O(2) = 3.996, and C(6)–O(3) = 4.578 Å. These distances are too large for appreciable hydrogen-bonding interactions. Furthermore, there are several factors of the present model which suggest that the C–H vector of the $CHCl_3$ solvate is not just sitting on the C_3 axis but is likely jumping to positions off the C_3 axis. First, the thermal ellipsoids for the three Cl atoms are severely elongated in a direction along the C_3 stacking axis. Second the C···C distance (1.418 Å) resulting from the disorder of the –CH moiety is longer than expected for a static 2-fold disorder of the $CHCl_3$ solvate molecule which would give a C···C distance of 1.18 Å. Thus, it is likely the chloroform C–H vector is involved in some off C_3 axis motion. It is, of course, not possible to have a unique definition of the $CHCl_3$ disorder from the X-ray structure.

Finally, the nature of intermolecular interactions between Fe_3O complexes in neighboring stacks needs to be highlighted. The three pyridine ligands of one Fe_3O complex overlap with the pyridine ligands of six neighboring Fe_3O complexes, two in each of the three neighboring stacks. Thus, there are stacks of pyridine ligands as

(15) Jang, H. G.; Thean, J. M.; Geib, S. J.; Rheingold, A. L.; Hendrickson, D. N. Unpublished results.

(16) Vincent, J. B.; Chang, H.-R.; Folting, K.; Huffman, J. C.; Christou, G.; Hendrickson, D. N. *J. Am. Chem. Soc.* **1987**, *109*, 5703.

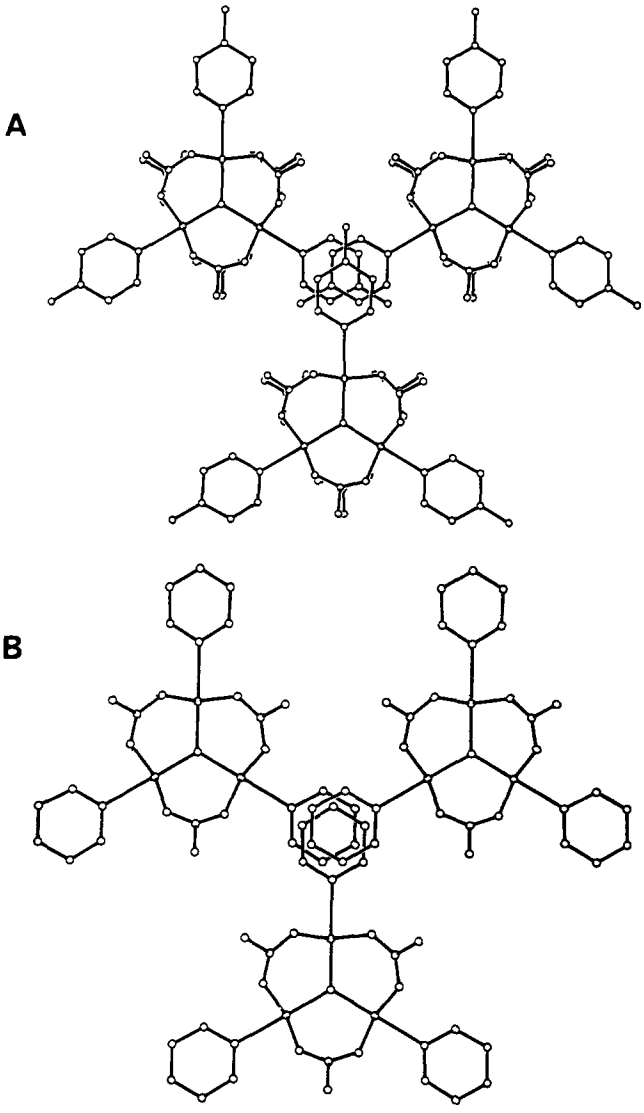

Figure 4. ORTEP view along c-axis of intermolecular pyridine–pyridine overlaps in (A) $[Fe_3O(O_2CCH_3)_6(4\text{-Me-py})_3](CHCl_3)$ (**1**) and (B) $[Fe_3O(O_2CCH_3)_6(py)_3](CHCl_3)$ (**5**).

well as stacks of Fe_3O complexes. The interplanar separation between pyridine ligands on neighboring complexes is c/3, which at 298 K is 3.458 Å for **1** and 3.496 Å for **5**. The appreciable pyridine–pyridine interaction expected at these close contacts is dimished somewhat by the poor alignment. In Figure 4 are given views of the pyridine–pyridine overlap in complexes **1** and **5**.

Thermal Effects Associated with Phase Transitions. DTA thermograms were run for complexes **1** and **2** in the temperature range of 85–300 K in order to identify where phase transitions occur. As can be seen in Figure 5, the $CHCl_3$ solvate **1** exhibits in a heating run one thermal anomaly with a peak at 95 K. The CH_3CCl_3 solvate **2** shows in the heating run one sharp peak at 125 K with a broad weaker feature at 129 K; in the cooling run complex **2** shows a peak at 125 K with a "shoulder" at ~128 K. Heat capacity measurements are planned for complex **1**.

The heat capacity under constant pressure, C_p, has been reported[5c,d] for $[Fe_3O(O_2CCH_3)_6(py)_3](py)$ (**6**) in the range of 12–300 K. Basically two phase transitions were observed. A first-order phase transition with two sharp C_p peaks at 111.4 and 112.0 K was seen, together with a higher order phase transition which evolves from ~113 K to culminate in two C_p peaks at 185.8 and 191.5 K. The total enthalpy and entropy of these phase transitions were determined by estimating plausible normal heat capacities to give ΔH = 4940 J mol^{-1} and ΔS = (30.58 ± 0.83)J K^{-1} mol^{-1}, respectively. In a later section a theoretical model for the origin of these phase transitions will be described.

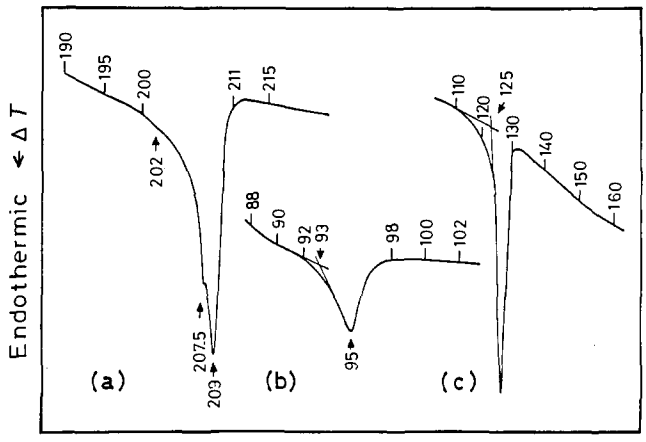

Figure 5. Heating DTA thermograms for the following: (a) $[Fe_3O(O_2CCH_3)_6(py)_3](CHCl_3)$; (b) $[Fe_3O(O_2CCH_3)_6(4\text{-Me-py})_3](CHCl_3)$; and (c) $[Fe_3O(O_2CCH_3)_6(4\text{-Me-py})_3](CH_3CCl_3)$.

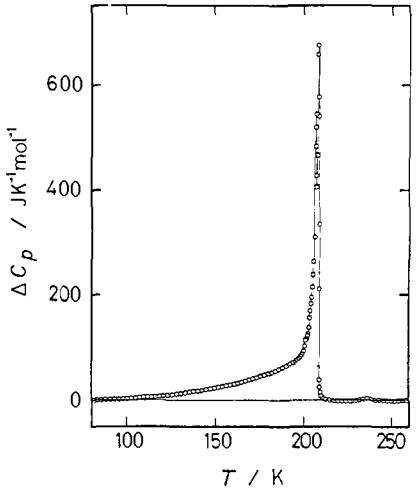

Figure 6. Excess heat capacity at constant pressure, ΔC_p, versus temperature for a 15.6245-g sample of $[Fe_3O(O_2CCH_3)_6(py)_3](CHCl_3)$ (**5**).

In the present study we determined C_p for a 15.6245-g sample of $[Fe_3O(O_2CCH_3)_6(py)_3](CHCl_3)$ (**5**) as a function of temperature in the range 14–300 K. Details of the measurements and data processing are available in another paper.[12] An effective frequency-distribution method[17] was employed to estimate a "normal" heat capacity curve. The difference between the observed and normal heat capacities is the excess heat capacity, ΔC_p, due to phase transitions. A plot of ΔC_p versus temperature is given in Figure 6, which shows that excess heat capacity begins to appear at temperatures above ~100 K. Two sharp ΔC_p peaks appear at 207.14 and 208.19 K. Above 208.19 K ΔC_p falls off abruptly without showing any appreciable thermal anomaly due to short-range ordering.

The total transition enthalpy (ΔH) and entropy (ΔS) arising from the phase transition(s) of complex **5** were determined by integration of ΔC_p with respect to T and ln T, respectively. The values calculated are ΔH = (5107 ± 44) J mol^{-1} and ΔS = (28.10 ± 0.44) J K^{-1} mol^{-1}. Because ΔS and ΔH are spread out over a substantial range of temperature, $\Delta G = \Delta H - T\Delta S$ does not equal zero. In Figure 7 is given a plot of ΔS versus temperature for complex **5**. For comparison purposes the previously reported[5d] ΔS data for the pyridine solvate **6** are also shown. There are three differences between the two ΔS versus temperature plots in Figure 7. First, the pyridine solvate exhibits an abrupt entropy gain somewhat less than Rln 2 at 112 K, whereas there is no evidence in the data for the $CHCl_3$ solvate of such a phase transition. Second, the total ΔS = 30.58 J K^{-1} mol^{-1} (~R ln 39.6) for the pyridine solvate exceeds the ΔS = 28.10 J K^{-1} mol^{-1} (~R ln 29.4)

(17) Sorai, M.; Seki, S. *J. Phys. Soc. Jpn.* **1972**, *32*, 382.

Table VI. ^{57}Fe Mössbauer Fitting Parameters for $[Fe_3O(O_2CCH_3)_6(py)_3](CHCl_3)$[a]

T (K)	δ,[b] mm/s			ΔE_Q, mm/s			Γ,[c] mm/s			% area		
	Fe^{III}	Fe^{av}	Fe^{II}	Fe^{III}	Fe^{av}	Fe^{II}	Fe^{III}	Fe^{av}	Fe^{II}	Fe^{III}	Fe^{av}	Fe^{II}
120	0.539 (1)		1.229 (1)	1.117 (1)		1.588 (2)	0.145 (1)		0.131 (2)	66.8 (1)		33.2 (1)
							0.143 (2)		0.138 (2)			
150	0.553 (1)		1.182 (1)	1.053 (1)		1.293 (2)	0.166 (2)		0.128 (4)	69.4 (1)		30.6 (1)
							0.150 (3)		0.143 (2)			
160	0.583 (9)	0.716 (9)	1.200 (4)	1.039 (2)	0.473 (2)	1.174 (3)	0.198 (4)	0.195 (5)	0.150 (6)	62.0 (1)	13.8 (1)	24.2 (1)
							0.195 (3)	0.223 (9)	0.181 (6)			
170	0.586 (9)	0.829 (6)	1.090 (8)	1.011 (2)	0.411 (9)	1.167 (6)	0.202 (9)	0.201 (4)	0.301 (9)	55.2 (1)	20.0 (1)	24.8 (1)
							0.159 (3)	0.327 (9)	0.218 (9)			
182	0.585 (2)	0.852 (2)	0.985 (2)	0.962 (5)	0.407 (4)	1.156 (5)	0.187 (3)	0.109 (6)	0.288 (9)	53.2 (1)	22.0 (2)	24.8 (2)
							0.196 (5)	0.100 (4)	0.152 (5)			
193	0.585 (9)	0.854 (9)	0.871 (6)	0.931 (2)	0.361 (9)	1.059 (1)	0.180 (4)	0.137 (6)	0.213 (9)	48.2 (1)	25.2 (2)	26.8 (1)
							0.162 (9)	0.142 (3)	0.225 (9)			
213		0.561 (1)			0.742 (1)			0.135 (1)			100 (1)	
								0.137 (1)				

[a] Peaks were least-squares fit to Lorentzian line shapes with equal areas for both components of a doublet; error in the last significant figure is given in parentheses. [b] Center shifts relative to Fe metal at room temperature. [c] Half-width at half-maximum listed in order of increasing velocity of the peak.

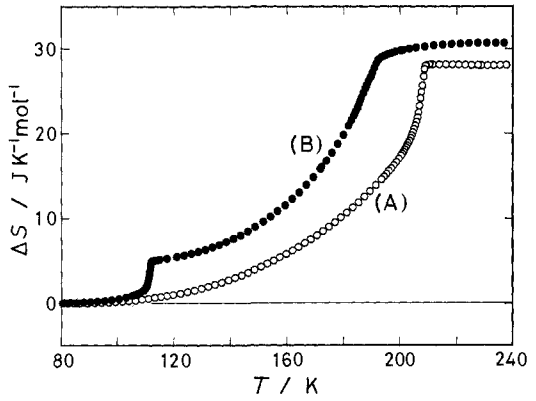

Figure 7. Acquisition of the transition entropy (i.e., ΔS) as a function of temperature for (A) $[Fe_3O(O_2CCH_3)_6(py)_3](CHCl_3)$ (**5**) and for (B) $[Fe_3O(O_2CCH_3)_6(py)_3](py)$ (**6**).

for the $CHCl_3$ solvate. The pyridine solvate seems to access more degrees of freedom. The third difference evident in Figure 7 is in the rate (slope) of entropy gain. In the case of the pyridine solvate the entropy gain above the 112 K phase transition is always gradual, whereas for the $CHCl_3$ solvate there is a relatively abrupt entropy gain as the temperature approaches the phase transitions at 207.14 and 208.19 K. It is appropriate to examine the ^{57}Fe Mössbauer and ^{2}H NMR data for these complexes before a model for the phase transitions in these complexes is discussed.

^{57}Fe Mössbauer Spectroscopy. Since heat capacity data have been determined for complexes **5** and **6**, the Mössbauer data for these two complexes should be viewed first. As was described in detail previously[5d] Mössbauer spectra have been reported for a ^{57}Fe-enriched sample of the pyridine solvate **6**. Examination of spectra taken at 1° intervals in the region of the 112 K first-order phase transition showed that at temperatures below 112 K there are two doublets, a high-spin Fe^{II} and a high-spin Fe^{III} doublet in the area ratio of 1:2. A third quadrupole-split doublet abruptly appears in the spectrum at 112 K. This third doublet corresponds to either a (Mössbauer) valence-detrapped or an electronically delocalized form of the Fe_3O complex. A "valence-detrapped" Fe_3O complex is one where the complex on the vibrational time scale (10^{-13} s) is trapped in one of three distorted $Fe^{II}Fe_2^{III}O$ vibronic states but is rapidly interconverting (tunneling) between the three $Fe^{II}Fe_2^{III}O$ vibronic states faster than the ^{57}Fe Mössbauer time scale (10^{-7} s). The third doublet for complex **6** was found[5g] to correspond to 30–40% of the spectral area between 112 and 168 K.

As the temperature of $[Fe_3O(O_2CCH_3)_6(py)_3](py)$ (**6**) is increased from 112 to ~185 K the three doublets in the Mössbauer spectrum change, eventually to become one average doublet somewhere in the 185–189 K range. This is interesting, for the higher order phase transition for **6** culminates with a C_p peak at

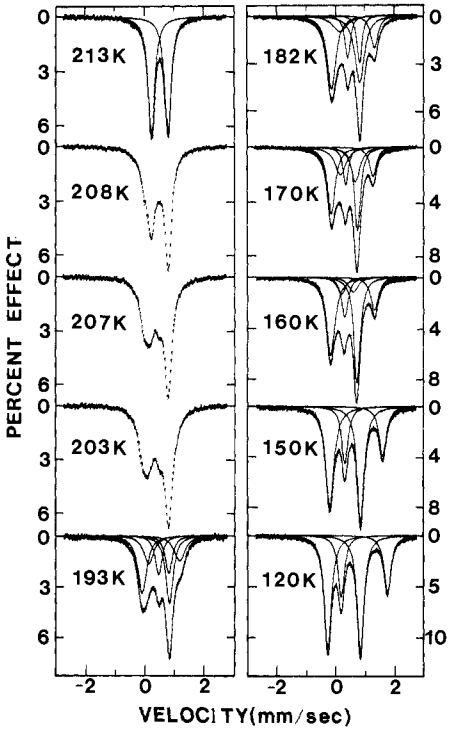

Figure 8. Variable-temperature ^{57}Fe Mössbauer spectra for $[Fe_3O(O_2CCH_3)_6(py)_3](CHCl_3)$ (**5**).

191.5 K. It was shown[5d] that this higher order phase transition in the ~113 to ~191.5 K range involves both an onset of lattice dynamics where the pyridine solvate molecule jumps between many sites and the Fe_3O complexes become valence detrapped.

In Figure 8 the temperature dependence of the Mössbauer spectrum for the $CHCl_3$ solvate **5** is illustrated. At temperatures below ~150 K there are two doublets, one for Fe^{II} and the other for Fe^{III} in an area ratio of ~1:2, respectively. Least-squares fitting parameters are given in Table VI. At ~160 K a third doublet appears in the spectrum; the third doublet at 160 K accounts for 13.8 (1)% of the spectral area. It reflects the appearance of some detrapped (delocalized) complexes. In the range of 160–193 K the amount of this third doublet increases from 13.8 (1) to 25.2 (2)% of the spectral area. Throughout this temperature range the components of the three doublets are moving together to become one average valence doublet, a process which appears to be completed at ~208 K. This is interesting for, as can be seen in Figure 6, the plot of ΔC_p versus temperature for $[Fe_3O(O_2CCH_3)_6(py)_3](CHCl_3)$ shows an abrupt drop after the peak at 208.19 K. Thus, as with complex **6**, valence detrapping of the Fe_3O complexes occurs cooperatively in a phase transition.

Table VII. ^{57}Fe Mössbauer Fitting Parameters for $[Fe_3O(O_2CCH_3)_6(4\text{-Me-py})_3](CHCl_3)$[a]

T (K)	δ,[b] mm/s			ΔE_Q, mm/s			Γ,[c] mm/s			% area		
	Fe^{III}	Fe^{av}	Fe^{II}	Fe^{III}	Fe^{av}	Fe^{II}	Fe^{III}	Fe^{av}	Fe^{II}	Fe^{III}	Fe^{av}	Fe^{II}
6	0.533 (1)		1.249 (1)	1.245 (1)		1.515 (2)	0.133 (2)		0.196 (2)	64.2 (1)		36.8 (1)
							0.141 (2)		0.196 (2)			
77	0.533 (1)		1.225 (2)	1.162 (2)		1.357 (4)	0.172 (2)		0.172 (4)	66.8 (1)		33.2 (1)
							0.157 (2)		0.215 (4)			
81	0.539 (1)	0.600 (9)	1.211 (2)	1.160 (2)	0.697 (9)	1.256 (3)	0.154 (2)	0.274 (6)	0.153 (3)	52.0 (1)	21.2 (4)	26.8 (1)
							0.139 (2)	0.228 (6)	0.207 (6)			
200		0.599 (1)			0.828 (1)			0.223 (1)			100 (1)	
								0.175 (1)				
298		0.555 (1)			0.767 (1)			0.146 (1)			100 (1)	
								0.146 (1)				

[a] Peaks were least-squares fit to Lorentzian line shapes with equal areas for both components of a doublet; error in the last significant figure is given in parentheses. [b] Center shifts relative to Fe metal at room temperature. [c] Half-width at half-maximum listed in order of increasing velocity of the peak.

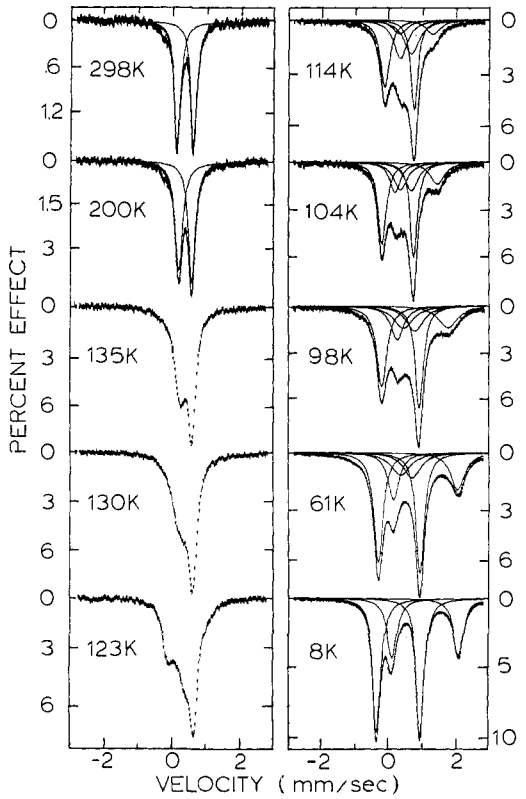

Figure 9. Variable-temperature ^{57}Fe Mössbauer spectra for $[Fe_3O(O_2CCH_3)_6(4\text{-Me-py})_3](C_6H_6)$ (4).

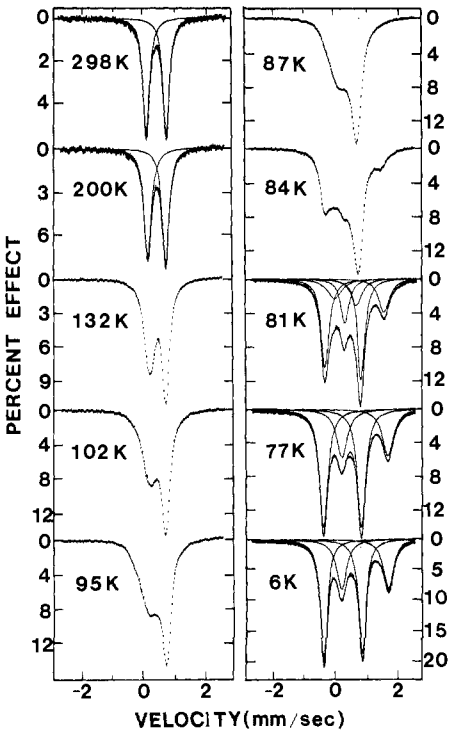

Figure 10. Variable-temperature ^{57}Fe Mössbauer spectra for $[Fe_3O(O_2CCH_3)_6(4\text{-Me-py})_3](CHCl_3)$ (1).

A comparison of the Mössbauer and ΔC_p data for complexes 5 and 6 is instructive. Pyridine solvate 6 shows a third doublet at ~112 K and a valence-detrapped doublet at 185–189 K in the Mössbauer spectrum. These temperatures correspond to those of the first-order phase transition and the culmination of the higher order phase transition. For the $CHCl_3$ solvate 5 the third doublet appears at ~160 K, and then at ~208 K there is only the one "detrapped" doublet. The latter temperature does correspond to the culmination temperature of the observed phase transition (two C_p peaks) for complex 5. However, there is no abrupt thermal effect seen at the temperature where the third doublet appears in the Mössbauer spectrum of 5. Thus, in contrast to the behavior of the pyridine solvate 6, the chloroform solvate 5 does *not* exhibit a phase transition at the temperature where the third detrapped doublet first appears. In the case of complex 5 there apparently is no cooperativity involved in this process, or there is a very correlated motion of Fe_3O complexes which considerably reduces the entropy gain associated with this process.

The temperature dependence of the Mössbauer spectrum of the benzene solvate 4 (see Figure 9) is similar to those for complexes 5 and 6. At temperatures below 60 K there are only two doublets present in an area ratio of 2:1. The third doublet for a detrapped species appears relatively suddenly at ~61 K. From 61 to 114 K the amount of this third doublet increases from 20.4 (1) to 38.6 (2)% of the spectral area. As can be seen in Figure 9, at ~130 K only the valence-detrapped doublet remains.

A very dramatic change in the variable-temperature Mössbauer characteristics occurs for $[Fe_3O(O_2CCH_3)_6(4\text{-Me-py})_3]S$ when the solvate molecule S is changed from benzene to $CHCl_3$. Spectra are presented for the $CHCl_3$ solvate 1 in Figure 10, and fitting parameters are given in Table VII. It is clear that this complex is valence trapped (two doublets) below 77 K. A third doublet characteristic of a detrapped complex appears in the 81 K spectrum. At temperatures above this the spectrum suddenly changes to one doublet such that by 87–95 K there is only the valence-detrapped doublet present. Thus, not only does this $CHCl_3$ solvate 1 become completely detrapped at ~35° lower temperature than the C_6H_6 solvate 4, but complex 1 converts from trapped to detrapped in a 15° range, whereas complex 4 changes over a 70° range. The one thermal anomaly seen in the DTA thermogram for complex 1 starts at ~91 K with a peak at ~95 K. Again there is good agreement between the changes seen in the Mössbauer spectrum and the temperature where a thermal anomaly is seen. The complex $[Fe_3O(O_2CCH_3)_6(4\text{-Me-py})_3](CHCl_3)$ is the first mixed-valence complex to show an abrupt transformation in its Mössbauer spectrum from valence trapped

Table VIII. ^{57}Fe Mössbauer Fitting Parameters[a] for Two Mixed-Valence Oxo-Centered Iron Acetates

T (K)	δ,[b] mm/s			ΔE_Q, mm/s			Γ,[c] mm/s			% area		
	Fe^{III}	Fe^{av}	Fe^{II}	Fe^{III}	Fe^{av}	Fe^{II}	Fe^{III}	Fe^{av}	Fe^{II}	Fe^{III}	Fe^{av}	Fe^{II}
					$[Fe_3O(O_2CCH_3)_6(4\text{-Me-py})_3](CH_3CCl_3)$ (**2**)							
100	0.478 (3)	0.715 (4)	0.991 (3)	0.977 (6)	0.503 (8)	1.672 (7)	0.126 (2)	0.264 (6)	0.158 (5)	33.2 (1)	45.4 (2)	21.4 (1)
							0.109 (2)	0.292 (7)	0.194 (5)			
110	0.475 (3)	0.722 (4)	0.960 (3)	0.919 (6)	0.426 (8)	1.547 (6)	0.138 (3)	0.262 (7)	0.135 (3)	34.2 (1)	46.8 (2)	19.0 (1)
							0.113 (2)	0.282 (8)	0.195 (7)			
118	0.479 (2)	0.734 (2)	0.949 (2)	0.868 (4)	0.360 (5)	1.453 (4)	0.157 (2)	0.255 (6)	0.123 (3)	34.0 (1)	48.0 (1)	18.0 (1)
							0.121 (5)	0.265 (6)	0.194 (6)			
240		0.517 (3)			0.708 (1)			0.147 (2)			100 (1)	
								0.148 (2)				
					$[Fe_3O(O_2CCH_3)_6(4\text{-Me-py})_3](CH_3CHCl_2)$ (**3**)							
110	0.449 (2)	0.730 (3)	0.926 (4)	0.960 (5)	0.398 (7)	1.629 (7)	0.112 (1)	0.268 (8)	0.175 (6)	38.6 (2)	41.8 (2)	19.4 (1)
							0.112 (1)	0.268 (8)	0.175 (6)			
240		0.641 (1)			0.579 (2)			0.267 (2)			100 (1)	
								0.216 (1)				
298		0.656 (1)			0.576 (3)			0.143 (2)			100 (1)	
								0.143 (2)				

[a] Peaks were least-squares fit to Lorentzian line shapes with equal areas for both components of a doublet; error in the last significant figure is given in parentheses. [b] Center shifts relative to Fe metal at room temperature. [c] Half-width at half-maximum listed in order of increasing velocity of the peak.

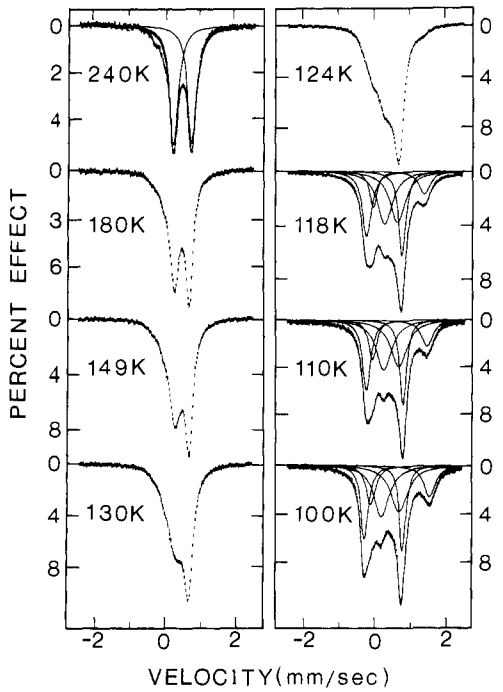

Figure 11. Variable-temperature ^{57}Fe Mössbauer spectra for $[Fe_3O(O_2CCH_3)_6(4\text{-Me-py})_3](CH_3CCl_3)$ (**2**).

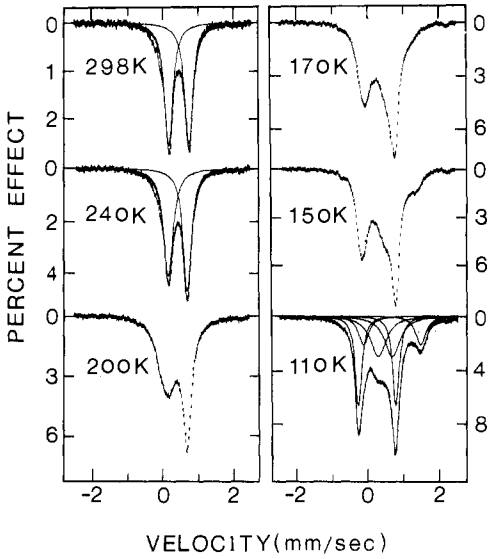

Figure 12. Variable-temperature ^{57}Fe Mössbauer spectra for $[Fe_3O(O_2CCH_3)_6(4\text{-Me-py})_3](CH_3CHCl_2)$ (**3**).

to detrapped. Either this complex has one phase transition at ~95 K, or there are two phase transitions, one at ~95 K (DTA) and the other at ~81 K where the third Mössbauer doublet appears. Heat capacity data are needed.

It was of interest to see what effect changing $CHCl_3$ (**1**) to CH_3CCl_3 (**2**) and then to CH_3CHCl_2 (**3**) has on the Mössbauer spectrum of $[Fe_3O(O_2CCH_3)_6(4\text{-Me-py})_3]S$. Spectra for the CH_3CCl_3 solvate **2** are shown in Figure 11. In the 100–118 K range each spectrum was fit (see Table VIII for parameters) to three doublets. The "valence-detrapped" doublet accounts for 45.4 (2)% of the spectral area at 100 K, and this increases slightly to 48.0 (1)% at 118 K. Since 100 K is the lowest temperature at which a spectrum was run for this complex, it is not known at what temperature the third doublet for the valence-detrapped species appears. The conversion from valence trapped to detrapped for complex **2** is, as with the $CHCl_3$ solvate **1**, occurring in a narrow temperature range; it is completed by ~124–130 K, as indicated by the Mössbauer data. This agrees with the DTA data which indicate a phase transition at ~125 K. Thus, the CH_3CCl_3 solvate requires a 30° higher temperature to valence detrap than does the $CHCl_3$ solvate **1**. This seems to be contrary to simple thoughts, for if the C–C vector of the CH_3CCl_3 solvate molecule lies along the C_3 stacking axis, it would have been expected that the larger size of CH_3CCl_3 compared to $CHCl_3$ would have reduced the interaction between Fe_3O complexes in neighboring stacks. The pyridine–pyridine interplanar separation between two Fe_3O complexes is equal to $c/3$ (c-axis is the stacking direction).

Mössbauer spectra were run for $[Fe_3O(O_2CCH_3)_6(4\text{-Me-py})_3](CH_3CHCl_2)$ (**3**) at six temperatures from 110 to 298 K, see Figure 12. Fitting parameters are given in Table VIII. The third valence-detrapped doublet is already present at 110 K as with complex **2**. Complex **3** has not become valence detrapped by 150 K. It takes a temperature of ~170 K to detrap fully this complex. It is pleasing to find that complex **3** with its less symmetric CH_3CHCl_2 solvate molecule valence detraps at a temperature which is ~45° higher than for the CH_3CCl_3 solvate **2**.

Solid-State ^{2}H NMR Spectroscopy. Generally there are two types of interactions apparent in the ^{2}H NMR spectrum of a paramagnetic compound. The nuclear quadrupole interaction of the ^{2}H ($I = 1$) nucleus gives rise to a doublet for each different deuteron site. Mixed-valence Fe_3O complexes are paramagnetic with an $S = 1$ ground state as well as appreciable thermal population in excited states at room temperature.[18] Thus, there can

be a through-space dipolar interaction of the magnetic moment associated with the unpaired electrons of the Fe_3O complex with the magnetic moment of the ^2H nucleus. As a result of this dipolar interaction the center of a ^2H NMR quadrupole-split doublet is shifted from zero frequency, which is defined as the ^2H NMR frequency for diamagnetic compounds. The dipolar interaction depends on the magnitude of the magnetic moment associated with the unpaired electrons and varies inversely with the cube of the distance between the nuclear and unpaired electron moments.

Solid-state ^2H NMR spectra of $[Fe_3O(O_2CCH_3)_6(py)_3](CDCl_3)$ are shown in Figure 13. Spectrum A is for an unoriented sample (powder) at 295 K, where the polycrystalline sample was suspended in fluid eicosane (mp = 38 °C) which was then cooled to form a wax block. In the case of spectra B, C, and D in Figure 13, a collection of ~20 small crystals of **5** were suspended in fluid eicosane and magnetically oriented[19] in the 8.45 T field, and then the eicosane was cooled to give a wax block. In the wax block the ~20 crystals were magnetically oriented so that their easy axes of magnetization were all aligned with the external field. In a previous study[5g] we showed that the easy axis of these *R*32 symmetry crystals is along the C_3 symmetry stacking axis (crystal *c*-axis).

Spectra B and C were run at 295 K with the external magnetic field aligned along or perpendicular to the C_3 symmetry stacking axis, respectively. Both of these spectra exhibit quite reasonable line widths (5 kHz), which indicate that the magnetic ordering in the wax block was very good. The quadrupole splitting observed in spectrum B is 196 kHz, whereas a splitting of 96 kHz is seen in spectrum C for the 90° orientation. Two conclusions can be immediately made from spectra B and C. First, at 295 K the residual quadrupole coupling tensor of the chloroform deuteron is within experimental error axially symmetric with its principal axis (∥ axis) directed along the C_3 symmetry stacking axis. Second, the chloroform C–D vector is not simply directed along the C_3 axis. The quadrupole splitting for the magnetic field parallel to the principal axis, $\Delta\nu_q(\|)$, is 244 kHz for pure solid $CDCl_3$, which is to say that the quadrupole coupling constant (Q_o) has been reported[20] to be 162.7 ± 1.0 kHz for $CDCl_3$. The observed value (196 kHz) of $\Delta\nu_q(\|)$ for complex **5** is considerably smaller than the 244 kHz value expected for a *static* C–D vector with the magnetic field parallel to the C–D vector. If α is the angle between the C–D vector and the external magnetic field, then the quadrupolar splitting observed is given by eq 1

$$\Delta\nu_q(\alpha) = \frac{3}{2}(e^2qQ/h)\,\frac{(3\cos^2\alpha - 1)}{2} \qquad (1)$$

From the above two conclusions it is clear that not only is the C–D vector of the $CDCl_3$ solvate molecule not directed parallel to the C_3 axis, but it must be dynamically moving about the C_3 axis such that it maintains the 3-fold symmetry.

In Figure 14 is shown the temperature dependence of the ^2H NMR spectrum for the magnetically oriented polycrystalline sample of complex **5** where the external magnetic field is parallel to the C_3 symmetry stacking axis. Above the ~208 K culmination temperature of the phase transition the experimental value of $\Delta\nu_q(\|)$ is essentially constant, ranging only from 196 to 204 kHz. When the sample temperature is decreased below the phase transition temperature, the value of $\Delta\nu_q$ decreases: 170 kHz at 193 K, 160 kHz at 153 K, and 144 kHz at 110 K. In the 223–295 K range the center (^2H chemical shift) of the quadrupole split doublet is shifted 39 kHz to low field. This corresponds to a ^2H chemical shift of 706 ppm downfield at 55.2 MHz. As the sample temperature is decreased below the phase transition temperature, the doublet shifts to even lower field. At 110 K the downfield shift is 123 kHz, which is equivalent to a 2228 ppm downfield chemical shift! Because there is only at most a very weak hydrogen bonding interaction of the C–D moiety of the chloroform solvate molecule with the paramagnetic Fe_3O complex, this very large chemical shift must be dominantly dipolar in nature. The 2228 ppm chemical shift is large compared to "isotropic" shifts seen for the ligands of paramagnetic complexes, which may be as large as 200–400 ppm.[21] The 2228 ppm shift rivals 2000–10000 ppm Knight shifts seen for protons in metallic solids.[22] Obviously, dipolar shifts seen for paramagnetic complexes in solution reflect an average of the magnetic anisotropy as a result of the rapid tumbling of the complex in solution. It is likely the $CDCl_3$ solvate molecule is fixed in orientation relative to a nearby Fe_3O complex at 110 K. Depending on the orientation of the C–D vector relative to the principal axis of the magnetic susceptibility tensor of the Fe_3O neighbor complex, the dipolar shift can be quite appreciable. Single-crystal ^2H NMR studies of paramagnetic complexes could prove to be of great utility in dealing with the long-standing question of separating Fermi contact and dipolar contributions to observed chemical shifts.

An explanation of the 196 kHz value of $\Delta\nu_q(\|)$ at 295 K and the decrease in $\Delta\nu_q(\|)$ as the temperature is decreased below 193 K can be given. At 295 K there are two possible models for the motion of the $CDCl_3$ solvate molecule which could account for the reduction of $\Delta\nu_q(\|)$ from the 244 kHz expected for a static C–D moiety directed along the C_3 axis to the experimental value of 196 kHz. In one model the C–D vector is positioned *not* along the C_3 axis but is taken as rapidly jumping between three equally probable positions, where in each position the C–D vector is directed perhaps at the two oxygen atoms in one acetate group. Because the $CDCl_3$ molecule sits on a 32 symmetry site, there are three positions of the C–D vector down and three positions up. In the case of fast motion compared to the quadrupole coupling constant, e^2qQ/h = 170 kHz, the eigen frequencies of H_Q are a weighted average according to the equilibrium distribution of molecular orientations $P(\theta,\phi)$,[23] where θ and ϕ are the Euler angles. For a discrete motional process, the average quadrupolar coupling tensor $\langle V_{ij}\rangle$ can be described by eq 2.

$$\langle V_{ij}\rangle = \sum P(\theta_k,\phi_k)V_{ij}(\theta_k,\phi_k) \qquad (2)$$

According to the quadrupole tensor averaging FORTRAN computer program[23] which diagonalizes eq 2, the angle α between the external magnetic field (collinear with the C_3 axis) and the C–D vector can be calculated to be α = 21.2° at 295 K for the first model.

In the second model for the disorder of the $CDCl_3$ solvate molecule, the C–D vector jumps rapidly between four positions of equal probability. (Actually, there are eight positions, four up and four down, however, there is no change in $\Delta\nu_q(\|)$ as a result of averaging about a C_2 axis which is perpendicular to the C_3 axis.) Three of these four positions are as described in the first model only the angle α is different. The fourth position would be where the C–D vector is along the C_3 axis. In this case the value of α is calculated[23] to be 24.7° at 295 K.

There are two reasons why the second model for the disorder of the $CDCl_3$ solvate molecule is preferred. As discussed above, the results of the X-ray structure indicate that the chloroform C–H···O contact distances to either the acetate O atoms (3.996 and 4.075 Å) or the central O^{2-} ion (4.578 Å) are large, and it is equally probable the C–H vector would point at the acetate O atoms as at the central O^{2-} ion. Further support for this second model of the disorder comes from the total observed entropy gain for the phase transition(s) of complex **5**. It was found that ΔS

(18) (a) Dziobkowski, C. T.; Wrobleski, J. T.; Brown, D. B. *Inorg. Chem.* **1981**, *20*, 671. (b) Tsukerblat, B. S.; Belinskii, M. I.; Kuyavskaya, B. Ya. *Inorg. Chem.* **1983**, *22*, 995. (c) Güdel, H. U. *J. Chem. Phys.* **1985**, *82*, 2510. (d) Cieplak, M. *Phys. Rev.* **1978**, *B18*, 3440. (e) Karpenko, B. V.; Kuznetsov, A. V. *Fiz. Met. Metalloved.* **1976**, *42*, 444. (f) Jones, D. H.; Sans, J. R.; Thompson, R. C. *J. Chem. Phys.* **1984**, *81*, 440. (g) Rakitin, Y. V.; Zhemchuzhnikova, T. A.; Zelentsov, V. V. *Inorg. Chim. Acta.* **1977**, *23*, 145. (h) Blake, A. B.; Yavari, A.; Hatfield, W. E.; Sethulekshmi, C. N. *J. Chem. Soc., Dalton Trans.* **1985**, 2509. (i) Oh, S. M., Ph.D. Thesis, University of Illinois, 1986.

(19) Rothgeb, T. M.; Oldfield, E. *J. Biol. Chem.* **1981**, *256*, 1432.

(20) Kunwar, A. C.; Gutowsky, H. S.; Oldfield, E. *J. Magn. Res.* **1985**, *62*, 521.

(21) *NMR of Paramagnetic Molecules*; LaMar, G. N., Horrocks, W. DeW., Holm, R. H., Eds.; Academic Press: New York, 1973.

(22) Knight, W. D. *Solid State Phys.* **1956**, *2*, 93.

(23) Wittebort, R. J.; Olejniczak, E. T.; Griffin, R. G. *J. Chem. Phys.* **1987**, *86*, 5411.

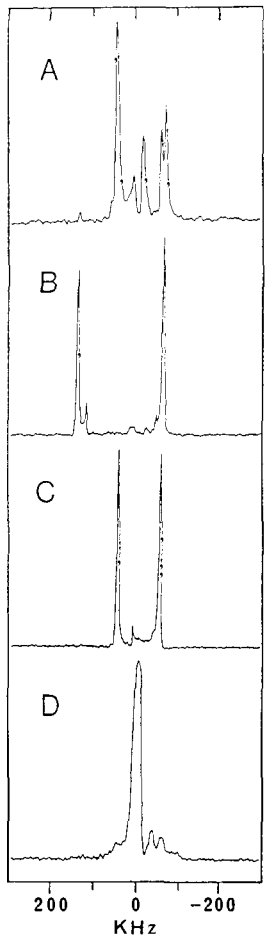

Figure 13. Solid-state ^2H NMR spectra for polycrystalline samples of $[Fe_3O(O_2CCH_3)_6(py)_3](CDCl_3)$ dispersed in an eicosane wax block with the following conditions: A, magnetically unoriented sample at 295 K; B, magnetically oriented sample at 295 K with the magnetic field parallel to the *c*-axis; C, magnetically oriented sample at 295 K with the magnetic field perpendicular to the *c*-axis; D, magnetically oriented sample at 110 K with the magnetic field perpendicular to the *c*-axis.

= 28.10 J K^{-1} mol^{-1} (= Rln 29.4). Each Fe_3O complex goes from valence trapped in one vibronic state at low temperatures to dynamically accessing all four vibronic states (three valence trapped and one delocalized, vide infra). This would give for the Fe_3O complex $\Delta S = R$ln 4. If the $CHCl_3$ solvate went from static at low temperature to dynamically moving between eight distinguishable lattice sites as proposed, then the solvate molecules would contribute $\Delta S = R$ln 8. This gives a total of $\Delta S = R$ln 4 + Rln 8 = Rln 32 (= 28.82 J K^{-1} mol^{-1}), which agrees with the experimental results.

The decrease in $\Delta\nu_q(\|)$ observed (Figure 14) as the temperature of complex **5** is decreased from 193 to 110 K is also explicable in terms of the above dynamical model for the $CDCl_3$ solvate molecules. As complex **5** is cooled below the phase transition, the motion of the $CDCl_3$ molecule slows down. The ΔS versus temperature curve in Figure 7 shows that entropy gain begins to appear at ~100 K as the compound is heated from 14 K. Thus, at 110 K the $CDCl_3$ solvate molecules are essentially static and sitting in *one* of the positions where the C–D vector is off the C_3 axis. Equation 1 can be used to calculate the angle α for this one position as $\alpha = 31.5°$. The α angle changes from 24.7° at 295 K for the three positions (i.e., three up and three down) off the C_3 axis to $\alpha = 31.5°$ for the one static position. The increase in α reflects an expected reduction in the in-stack distance between Fe_3O complexes (i.e., *c*-axis) as the crystal contracts.

Finally, spectrum D in Figure 13 is for the wax block of magnetically oriented crystals maintained at 110 K. In this case the wax block has been turned so that the magnetic field makes an angle of 90° with the easy axis of magnetization. That is, the magnetic field is perpendicular to the stacking axis. In this spectrum we see a single broad resonance centered at zero frequency with a full width at half height of ~20 kHz. The C–D vector locks down into the $\alpha = 31.5°$ single position at 110 K. There is good order only along the easy axis of magnetization; however, in the plane perpendicular to this easy axis there is no ordering. Thus, when the C–D vector locks into one position at $\alpha = 31.5°$, throughout the sample of ~20 crystals, each with its presumed domain structure, there is effectively a cone at 31.5° about the easy axis where the C–D vectors are located. When the magnetic field is turned to 90° from the easy axis, there is then a distribution of C–D vector directions relative to the magnetic field direction. This distribution runs from the complementary angle of 31.5°, i.e., 58.5°, to a value of 90°. Naively, we would have expected a pseudopowder-type spectrum where the angular distribution ran from $\alpha = 58.5°$ to $\alpha = 90°$. However, spectrum D in Figure 13 only shows one broad feature. This broad feature does approximate the type of signal expected for molecules with $\alpha = 58.5°$, for this angle is close to the magic angle where $(3\cos^2\alpha - 1) = 0$ and $\Delta\nu_q$ would be expected to be zero. It is not clear why we only see this signal, but it is important to remember (spectrum A in Figure 13) that for these paramagnetic compounds even a powder sample dispersed in a wax matrix does *not* give a powder spectrum. Only sharp single-crystal type signals are seen for the turning points (i.e., parallel and perpendicular directions of the qcc tensor). The 90° turning point features may be difficult to observe, for this doublet would be appreciably dipolar shifted. It is satisfying that the broad feature which is seen is essentially at zero frequency, for not only the $\Delta\nu_q$ value but also the dipolar shift would be expected to be minimized with α close to the magic angle.

Nature of Phase Transitions. A potential energy surface for a single mixed-valence Fe_3O complex is calculated[5f,24-26] by linearly coupling a three-site tight-binding model for the extra electron in the complex to the e_g symmetry Fe_3O stretching vibration. The electronic basis set consists of the functions ϕ_A, ϕ_B, and ϕ_C, where ϕ_A means the extra electron is on the Fe_A site. The e_g vibration can be represented[5f] as having the normal coordinates Q_u and Q_v, which can be written in the polar coordinates q and θ as $Q_u = q\cos\theta$ and $Q_v = q\sin\theta$. The appearance of the potential energy surfaces for the vibronic states in this complex depends on the values of the electronic coupling, ϵ, between two iron ions (i.e., tunneling matrix element) and the vibronic coupling energy, λ^2/k, where k is the force constant for the e_g stretching vibration and λ is the vibronic coupling constant of d electrons to the e_g vibrational mode. When these two energies are of comparable magnitude and $\Delta(= k\epsilon/\lambda^2)$ is in the range of $2/3 < \Delta < 0.765$, then the energies of the three vibronic states, $E_i(q,\theta)$, as a function of q appears as shown in Figure 15A. In this drawing a cut of the potential energy diagram is shown where the distortion (q) is along the direction $\theta = \theta_o$ of one Fe–O(oxide) bond. There are two excited states. The potential energy surface for the ground state has four minima at $(q_o,0)$, $(q_o,\pm 2\pi/3)$, and (0,0) for $2/3 < \Delta < 0.765$. The appearance of this ground-state surface for $\Delta = 0.74$ is shown in Figure 15B. The first three minima correspond to localized states where the extra d electron is localized largely on the Fe ion at the A, B, and C sites. The minimum at (0,0), which means an undistorted molecule, corresponds to an electronically delocalized vibronic state.

In the solid state there are appreciable intermolecular interactions between Fe_3O complexes in the six $R32$ symmetry complexes studied in this paper. A schematic view down the stacking axis of the packing arrangement for these complexes is shown in Figure 16. One Fe_3O complex, the central one, is shown surrounded by six Fe_3O complexes in the neighboring stacks. It is evident from this drawing that there are appreciable intermolecular interactions as a result of the overlap of pyridine ligands between

(24) Launay, J. P.; Babonneau, F. *Chem. Phys.* **1982**, *67*, 295.
(25) Borshch, S. A.; Kotov, I. N.; Bersuker, I. B. *Chem. Phys. Lett.* **1982**, *89*, 381.
(26) Cannon, R. D.; Montri, L.; Brown, D. B.; Marshall, K. M.; Elliot, C. M. *J. Am. Chem. Soc.* **1984**, *106*, 2591.

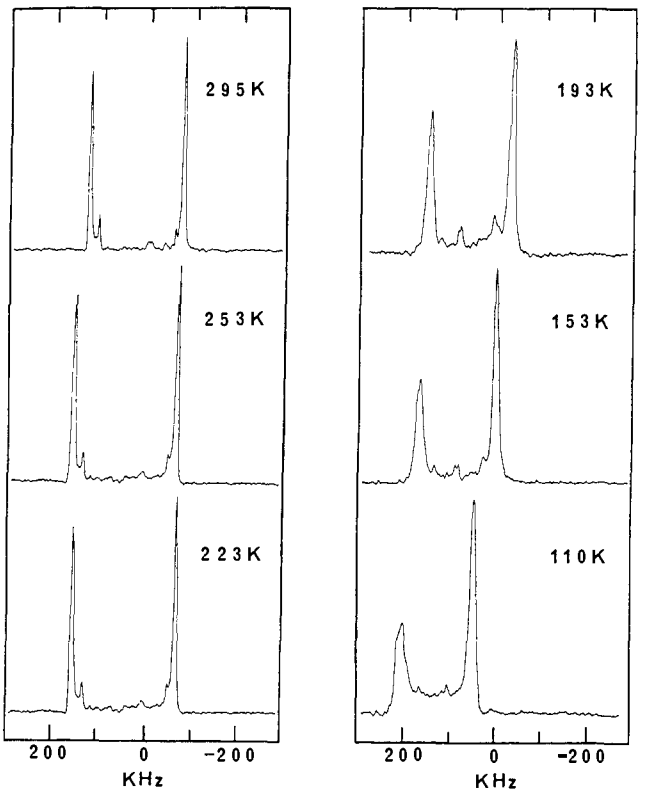

Figure 14. Temperature dependence of the solid-state ^2H NMR spectrum of eicosane wax-embedded magnetically oriented collection of ~20 small crystals of $[Fe_3O(O_2CCH_3)_6(py)_3](CDCl_3)$. The magnetic field is oriented parallel to the *c*-axis (stacking axis) of crystals.

Fe_3O complexes. Not only are there stacks of Fe_3O complexes, but there are also stacks of pyridine ligands. The solvate molecules are sandwiched between Fe_3O complexes in each stack of Fe_3O complexes. Before the pyridine–pyridine intermolecular interactions are highlighted, it is appropriate to describe a model for the phase transitions in these complexes.

The first statistical mechanical model to describe the phase transitions observed for mixed-valence Fe_3O complexes was proposed by Kambara et al.[5f] The effect of solvate molecule dynamics was ignored. Intermolecular interactions were treated with the molecular field approximation. Three types of phase transitions were delineated: (1) order–disorder transition with respect to the alignment of the sense of valence-trapped (i.e., distorted) complexes; (2) static localization–delocalization transition where the molecular distortion disappears above the transition temperature and electrons are coherently delocalized on the three Fe ions; and (3) dynamical localization–delocalization transition in which the delocalization comes from the fast electron transfer between the three Fe ions in a Fe_3O complex and the molecular structure is changed from a static distortion to a dynamical distortion. The possibility of the condensed phase modulating the potential energy surface of the ground state was considered; however, it was not possible to find a set of parameters which, for example, explained quantitatively the ΔS versus temperature and Mössbauer results for the two phase transitions observed for $[Fe_3O(O_2CCH_3)_6(py)_3](py)$.

Stratt and Adachi[8] took an imaginative and insightful approach to developing a theoretical model for the phase transitions in the mixed-valence Fe_3O complexes. Again the effects of solvate molecule dynamics was ignored. They assumed the same type of intermolecular interactions exist between nearest neighbor complexes as were assumed by Kambara et al.[5f] However, they employed a "spin" type Hamiltonian, in analogy with treatments of phase transitions in magnetic exchange interacting systems. This second model in essence restricts the phase space compared to the earlier model; however, this second model leads logically to the idea of two interpenetrating sublattices of Fe_3O complexes. The phase transitions in antiferromagnets,[27] and cooperative

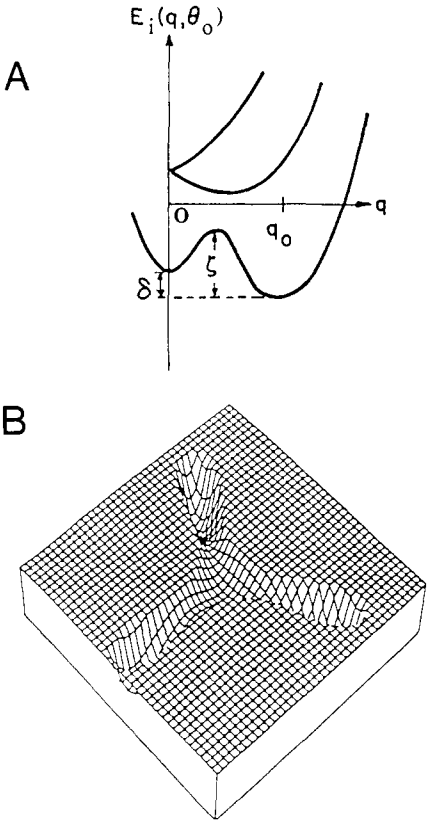

Figure 15. (A) Plot of energies $E_i(q,\theta_o)$ of the three vibronic states of an isolated mixed-valence Fe_3O complex as a function of the distortion along one Fe–O(oxide) bond. There are two excited states and one ground state. The parameter δ gauges the difference in zero-point energies of distorted and delocalized states, and ζ gauges the barrier height for a complex which is thermally activated to convert from the distorted vibronic state to the electronically delocalized state. (B) Potential energy surface for $\Delta = 0.74$ of ground state of isolated Fe_3O complex showing the four minima which occur when the electronic and vibronic couplings are comparable. Note the one minimum at the origin of the surface; this minimum corresponds to an undistorted, electronically delocalized vibronic state of the complex.

Jahn–Teller[28,29] systems can be described in terms of two interpenetrating sublattices. Thus, each Fe_3O complex in sublattice A is surrounded by six Fe_3O complexes which are in sublattice B and vice versa.

In Figure 17 is shown the phase diagram developed by Stratt and Adachi.[8] The interaction energies 0, J_1, J_2, and J_3 are, respectively, the energies of two neighboring complexes, both of which are undistorted; both of which are distorted parallel to each other; only one of which is distorted; and both of which are distorted but at an angle of $2\pi/3$ with respect to each other. The phase diagram in Figure 17 was calculated by assuming $J_3/J_1 = 0.25$. The existence of three different phases was automatically predicted, where these three phases can be described as the following: **Phase I** (Ferrodistortive Phase): All complexes are valence localized, and because of strain dipoles the sense of distortion of each Fe_3O complex is the same. **Phase II** (Antiferrodistortive Phase): Two interpenetrating sublattices exist where one sublattice has valence localized complexes and the sense of distortion is random. The other sublattice has an appreciable number of undistorted (delocalized) complexes mixed with randomly oriented localized complexes. **Phase III** (Paradistortive Phase): Random distribution of distorted and undistorted complexes. Each Fe_3O complex is probably dynamically transferring between its four

(27) Morrish, A. H. *Physical Principles of Magnetism*; John Wiley and Sons: New York, 1965.
(28) Bersuker, I. B. *The Jahn-Teller Effect and Vibronic Interactions in Modern Chemistry*; Plenum Press: New York, 1984.
(29) (a) Gehring, G. A.; Gehring, K. A. *Rep. Prog. Phys.* **1975**, *38*, 1. (b) Reinen, D.; Friebel, C. *Structure and Bonding* **1979**, *37*, 1.

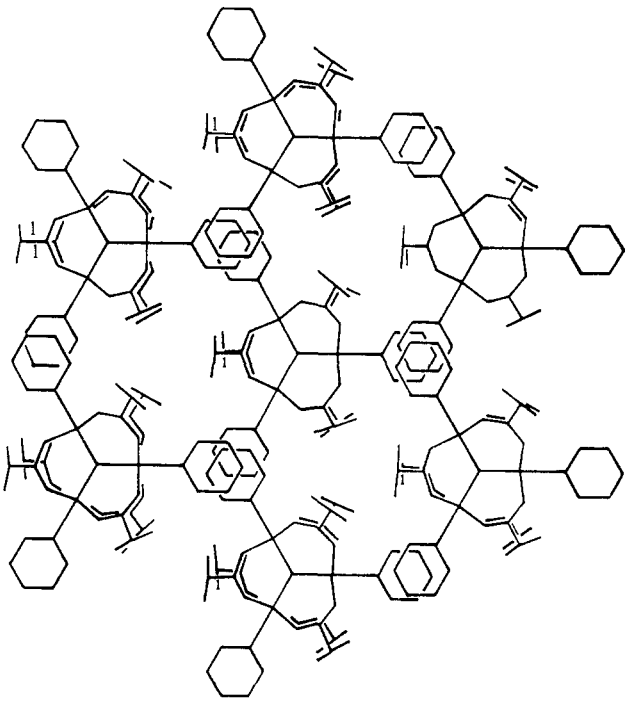

Figure 16. Schematic view down the stacking axis (c-axis) of the packing arrangement for the $R32$ space group complexes **1**–**6**.

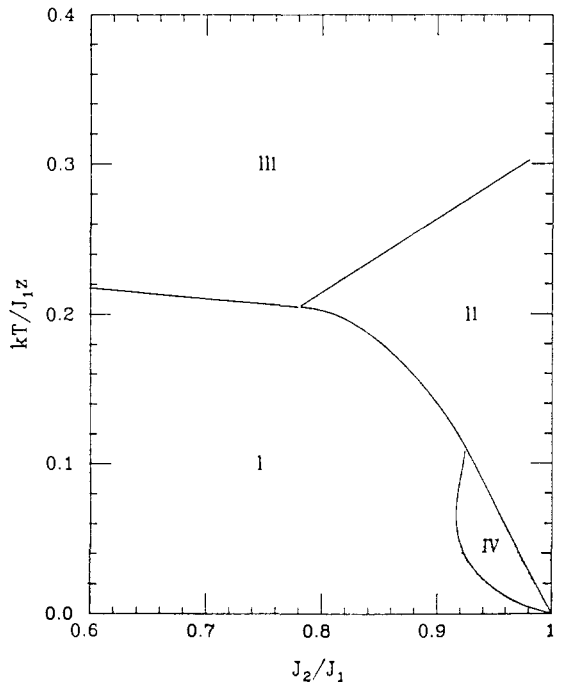

Figure 17. Phase diagram calculated by Stratt and Adachi[8] employing a molecular field theory to account for the phase transitions in mixed-valence Fe_3O complexes which crystallize in the $R32$ space group. The vertical axis is temperature plotted in units of J_1z/k, where k is the Boltzmann constant, z is the number of Fe_3O complexes surrounding each Fe_3O complex, and J_1 is the interaction energy of two neighboring complexes, both of which are distorted parallel to each other. The horizontal axis is the ratio of the "antiferromagnetic" (J_2) to the "ferromagnetic" (J_1) coupling, where J_2 is the interaction energy for two neighboring complexes, one of which is distorted and the other is undistorted.

vibronic states. Stratt and Adachi also noted the possibility of a fourth phase which they described as having two sublattices as in phase II but with both sublattices "ferromagnetic" and distorted in the same direction. It is important to note that only the phase boundary between I–III, I–II, and IV–II phases gives first-order transitions. The remainder are second order.

The phase diagram of Stratt and Adachi[8] does seem to account for the observations on $[Fe_3O(O_2CCH_3)_6(py)_3](py)$. If J_2/J_1 was in the range of ~0.8–0.9, then increasing the temperature from 0 K would lead to a first-order I → II phase transition, followed by a second-order II → III phase transition which would culminate at the boundary line between the II and III phases. In the heat capacity data[5d] for this compound there is a first-order transition at 112 K, followed by a higher order phase transition which starts at ~113 K and culminates at ~191 K. The abrupt appearance in the Mössbauer spectrum of a third doublet characteristic of an undistorted complex (30.4% of the spectral area) at 112 K also fits the theory. By the time the temperature is increased to ~191 K there is only a doublet for valence-detrapped Fe_3O complexes present. Each Fe_3O complex is tunneling faster than $\sim 10^8$–10^9 s^{-1} between its four vibronic states above ~191 K.

In contrast to the case for the pyridine solvate complex **6**, only one phase transition has been detected for the other complexes. In DTA thermograms, complexes **1** and **2** have phase transitions at 95 and ~125 K, respectively. These are the temperatures where these two complexes become valence detrapped on the Mössbauer time scale. In the heat capacity data for $[Fe_3O(O_2CCH_3)_6(py)_3](CHCl_3)$ (**5**) only one phase transition at ~208 K is seen. Again, this is the temperature where the valence detrapping occurs. If the Stratt–Adachi phase diagram applies to these complexes, then it is possible that these complexes are only involved in one phase transition from phase I to phase III. This phase transition should be of first order. No hysteresis was seen in the DTA thermogram for complex **5**. The appearance of the C_p versus temperature data does suggest the presence of some first-order component to the phase transition of complex **5**. However, it cannot be definitively stated what order this phase transition is. In fact, there is no direct evidence for the presence of two interpenetrating sublattices in any of the mixed-valence Fe_3O complexes, and, thus, the applicability of the Stratt–Adachi phase diagram is still to be established. It is also not known why complex **5** shows a rather abrupt appearance of a third doublet in the Mössbauer spectrum at ~160 K, yet there is no evidence of a thermal effect, and therefore a phase transition, at this same temperature.

Very recently the heat capacity of $[Mn_3O(O_2CCH_3)_6(py)_3](py)$ was measured.[30] This compound only shows one phase transition at 185 K. The entropy gain (~Rln 72) occurs in a narrow temperature range. From the appearance of the C_p versus T data this phase transition clearly seems to be first order. This is interesting for this Mn_3O complex is known[16] to be isostructural to the Fe_3O complex **6**. It is possible that the Mn_3O complex only makes a first-order transition from the ferrodistortive phase I to the paradistortive phase III. The c-axis of the Mn_3O complex (c = 10.918 (3) Å) at 223 K is only a little larger than the c-axis (c = 10.853 (3) Å) of the Fe_3O complex **6**.

Since we have only been able to determine the single-crystal X-ray structures of complexes **1**, **4**, **5**, and **6** at temperatures corresponding to the paradistortive phase III, it is not possible to evaluate all four of the interaction parameters (O, J_1, J_2, and J_3) from crystallographic coordinates. Furthermore, the structure determinations for **4** (133 K) and **6** (200 K) were carried out at much lower temperatures than the 298 K value used for complexes **1** and **5**. A variation in the unit cell parameters would lead to changes in the intermolecular interaction parameters. Detailed temperature-dependent X-ray and neutron diffraction studies are needed.

As a semiquantitative guide of the magnitude of the variation of the intermolecular interactions in complexes **1**, **4**, **5**, and **6** CNDO/2 molecular orbital calculations were carried out. The approximate value for the intermolecular pyridine–pyridine overlap was evalued with CNDO/2 calculations for these four complexes. Atomic coordinates were taken from the crystallographic results. In each case a calculation of the total electronic energy was carried out both for two pyridine ligands overlapping as pictured in Figure

(30) Nakano, M.; Sorai, M.; Vincent, J. B.; Christou, G.; Hendrickson, D. N. Manuscript in preparation.

4 for complexes **1** and **5** and for only one pyridine ligand. The difference between the former total electronic energy and two times the energy for a single pyridine gave an estimate of the interaction energy. This is the interaction between two *undistorted* Fe_3O complexes as a result of their two pyridine ligands overlapping. The values for the interaction energies are as follows: 0.44 Kcal/mol for C_6H_6 solvate **4**; 0.88 kcal/mol for pyridine solvate **6**; 1.11 kcal/mol for $CHCl_3$ solvate **5**; and 1.22 kcal/mol for the $CHCl_3$ solvate **1**. This is a variation of 0.78 kcal/mol (= 270 cm^{-1}), a quantity which is comparable to the quantum of the e_g Fe_3O stretching mode which is coupled to the electronic coordinates in these complexes.

Concluding Comments

For the series of *R*32-symmetry complexes $[Fe_3O(O_2CCH_3)_6(L)_3]S$ onset of intramolecular electron transfer occurs cooperatively in a phase transition. It seems likely that changing the solvate molecule leads to changes in the intermolecular interactions via the pyridine-pyridine overlaps.

It is also generally found that the onset of dynamics of the solvate molecule occurs in the same phase transition which involves an increase in the rate of electron transfer. Since the phase transition is a cooperative process, it is not perhaps appropriate to ask whether the onset of solvate molecule motion causes an increase in the rate of electron transfer or vice versa. However, it is fascinating that even a solvate molecule such as the C_3 symmetry $CHCl_3$ molecule moves seemingly synchronously with the vibronic coordinate changes occurring in neighboring Fe_3O molecules in complex **5**.

The van der Waals interaction between a solvate molecule S which is positioned asymmetrically relative to the C_3 axis of a nearby Fe_3O complex may lead to an interaction energy of only 10-100 cm^{-1} per solvate molecule. However, this amount of $Fe_3O\cdots S$ interaction may be large enough to modify the ground-state potential energy surface for a Fe_3O complex to appreciably affect the rate at which such a complex can tunnel from one vibronic minimum to another. It would be very instructive if one could employ laser flash photolysis on an asymmetric complex such as $[Co^{II}Fe_2^{III}O(O_2CCH_3)_6(py)_3](py)$ to measure the rate of electron transfer ($Co^{II} \rightarrow Fe^{III}$) as a function of whether the pyridine solvate molecules are or are not rapidly jumping between the three positions on the C_3 axis. We have already established[31] with heat capacity measurements on this $Co^{II}Fe_2^{III}O$ complex that it does have a phase transition which involves the onset of pyridine solvate dynamics.

Acknowledgment. We are grateful for support from National Institutes of Health Grant HL13652 (D.N.H.). M.S. expresses his sincere thanks to the Ministry of Education, Science and Culture for a Grant-in-Aid for Scientific Research. D.N.H. is grateful to Professor Richard Wittebort for useful comments and to Professor Eric Oldfield for help with the ^2H NMR experiments (work supported in part by NIH Grant HL19481).

Supplementary Material Available: Tables of bond lengths and angles, anisotropic thermal parameters, and hydrogen atom coordinates and thermal parameters for $[Fe_3O(O_2CCH_3)_6(4\text{-Me-py})_3(CHCl_3)$ (**1**) and $[Fe_3O(O_2CCH_3)_6(py)_3](CHCl_3)$ (**5**) (3 pages); listings of structure factor amplitudes for **1** and **3** (15 pages). Ordering information is given on any current masthead page.

(31) Sorai, M.; Kaji, K.; Jang, H. G.; Hendrickson, D. N. Manuscript in preparation.

Co(III) Complex Promoted Hydrolysis of Phosphate Diesters: Comparison in Reactivity of Rigid *cis*-Diaquotetraazacobalt(III) Complexes

Jik Chin,* Mariusz Banaszczyk, Vrej Jubian, and Xiang Zou

Contribution from the Department of Chemistry, McGill University, Montreal, Canada H3A 2K6.
Received February 23, 1988. Revised Manuscript Received August 8, 1988

Abstract: The efficiencies of three rigidly held *cis*-aquohydroxotetraazacobalt(III) complexes $[(cyclen)Co(OH)(OH_2)]^{2+}$, $[(tren)Co(OH)(OH_2)]^{2+}$, $[(trpn)Co(OH)(OH_2)]^{2+}$ in promoting the hydrolysis of bis(*p*-nitrophenyl)phosphate (BNPP) have been compared. In neutral water at 50 °C, the rate constant for hydrolysis of the phosphate diester bond in $[(cyclen)Co(OH)(BNPP)]^+$, $[(tren)Co(OH)(BNPP)]^+$, $[(trpn)Co(OH)(BNPP)]^+$ are 4.6×10^{-1}, 8.1×10^{-3}, and 2.5 s^{-1}, respectively. $[(trpn)Co(OH)(BNPP)]^+$ is hydrolyzed at about the same rate as BNPP bound to a real enzyme from *Enterobacter aerogenes* and about 10^{10} times more rapidly than free BNPP. The dramatic increase in the activity of the Co(III) complex with change in the tetraamine ligand structure can be explained in terms of a detailed mechanism of the reaction.

Currently there is considerable interest in developing catalysts that can cleave DNA sequence specifically. Due to the stability of the DNA phosphate diester backbone toward hydrolytic cleavage, emphasis to date has been mainly focused on oxidative cleavage of DNA.[1] A major challenge remains in developing catalysts that can cleave DNA hydrolytically.[2] We recently showed that Co(III) complexes can be by far the most efficient in promoting the hydrolysis of phosphate diesters with good[3] or poor leaving groups.[4] Interestingly, the activity of the cobalt complexes is sensitive to the tetraamine ligand structure. For

(1) (a) Barton, J. K. *Science (Washington, D.C.)* **1986**, *233*, 727-734. (b) Sigman, D. S. *Acc. Chem. Res.* **1986**, *19*, 180-186. (c) Dervan, P. B. *Science (Washington, D.C.)* **1986**, *232*, 464-471. (d) Moser, H. E.; Dervan, P. B. *Ibid.* **1987**, *238*, 645-650. (e) Corey, D. R.; Schultz, P. G. *Ibid.* **1987**, *238*, 1401-1403. (f) Chen, C. B.; Sigman, D. S. *Ibid.* **1987**, *237*, 1197-1201.

(2) (a) Dervan, P. B. *Chem. Eng. News* **1988**, (*Jan. 4*), 25. (b) Basile, L. A.; Barton, J. K. *J. Am. Chem. Soc.* **1987**, *109*, 7548-7550. (c) Basile, L. A.; Raphael, A. L.; Barton, J. K. *J. Am. Chem. Soc.* **1987**, *109*, 7550-7551.

(3) (a) Chin, J.; Zou, X. *J. Am. Chem. Soc.* **1988**, *110*, 223-225. (b) Chin, J.; Banaszczyk, M.; Jubian, V. *J. Chem. Soc., Chem. Commun.* **1988**, 735-736.

(4) Chin, J.; Zou, X. *Can. J. Chem.* **1987**, *65*, 1882-1884.

0002-7863/89/1511-0186$01.50/0